Burns & Trauma, 2026, **14**, tkag002
https://doi.org/10.1093/burnst/tkag002
Published: 6 January 2026
Research Article

OXFORD

Spatiotemporal regulation of acute wound healing by the NLRP3 inflammasome: dual roles in macrophage-fibroblast chemotaxis and phenotype during wound repair

Dongzhen Zhu[1,2,‡], JianJun Li[1,2,3,‡], Bingyang Yu[1,4,‡], Nanbo Liu[5,‡], Xu Guo[1], Yanlin Su[1], Yuzhen Wang[1], Yuyan Huang[1,2], Liting Liang[1,2], Linhao Hou[1], Chao Zhang[1], Qinghua Liu[1], Mengde Zhang[1,2], Wei Song[1], Yi Kong[1], Jinpeng Du[1], Zhao Li[1], Yue Kong[1], Feng Tian[1], Xiangye Yin[1,2], Ping Zhu[5], Xiaobing Fu[1,2,*], Sha Huang[1,2,*]

[1]Research Center for Wound Repair and Tissue Regeneration, Medical Innovation Research Department, Chinese People's Liberation Army General Hospital, 51 Fucheng Road, Haidian District, Beijing 100048, China
[2]Chinese People's Liberation Army Medical School, 28 Fuxing Road, Haidian District, Beijing 100853, China
[3]Department of General Surgery, The Six Medical Centre, Chinese People's Liberation Army General Hospital, 28 Fu Xing Road, Haidian District, Beijing 100853, China
[4]Department of Biomaterial, College of Life Sciences, Mudanjiang Medical University, 3 Tongxiang Street, Aiming District, Mudanjiang 157011, China
[5]Guangdong Cardiovascular Institute, Guangdong Provincial People's Hospital (Guangdong Academy of Medical Sciences), Southern Medical University, 106 Zhongshan 2nd Road, Yuexiu District, Guangzhou, Guangdong 510100, China

*Corresponding authors. Xiaobing Fu, E-mail: fuxiaobing@vip.sina.com; Sha Huang, E-mail: stellarahuang@sina.com
‡Dongzhen Zhu, JianJun Li, Bingyang Yu, and Nanbo Liu contributed equally to this work.

Abstract

Background: The spatiotemporal regulation of inflammatory dynamics is critical for successful wound healing. However, the precise mechanistic role of the NOD-like receptor family pyrin domain-containing 3 (NLRP3) inflammasome in orchestrating these processes remains incompletely characterized. This study aimed to delineate the specific mechanisms by which NLRP3 governs cellular and molecular events during wound healing.

Methods: Multi-omics sequencing data were utilized to profile NLRP3 inflammasome activation dynamics in murine and human acute wound models. Nlrp3−/− mice were generated using CRISPR-Cas9 technology. *In vitro* and *in vivo* functional assays were performed to assess NLRP3-dependent regulation of macrophage and fibroblast recruitment, polarization, and phenotype modulation.

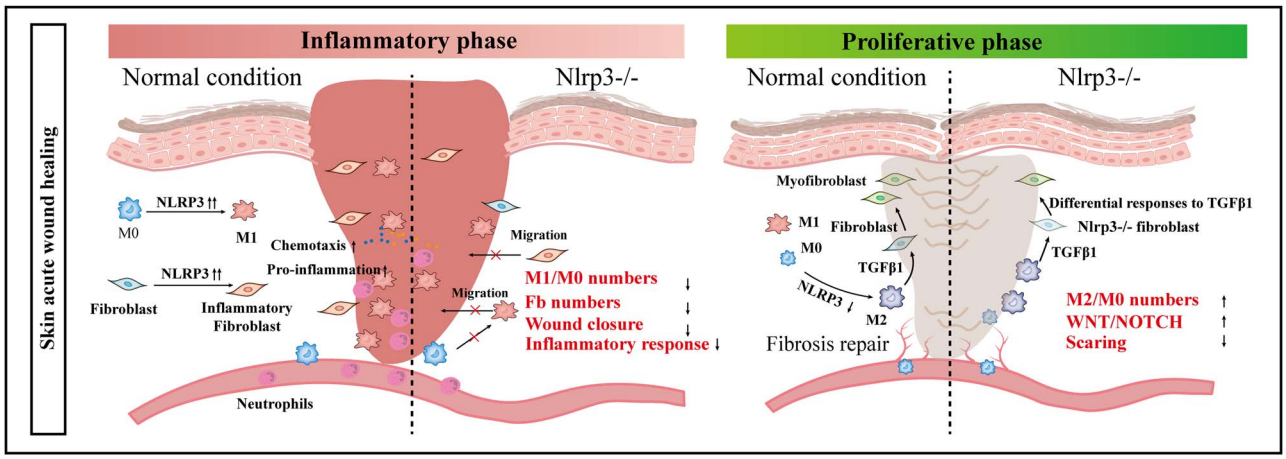
Results: NLRP3 is predominantly expressed in macrophages and neutrophils during the inflammatory phase of wound healing. Global deletion of Nlrp3 reduces IL-1β, the main downstream effector, attenuates CCL/CXCL chemokine signaling, decreases both inflammatory and pro-reparative cell infiltration, and disrupts the phenotypic switching of macrophages and fibroblasts, collectively delaying wound closure. However, the resulting low-inflammatory microenvironment in Nlrp3−/− mice may upregulate Wnt and Notch signaling early in the repair phase, curbing fibrosis and promoting appendage regeneration. Partial IL-1β blockade in WT mice recapitulates the NLRP3-null phenotype, whereas IL-1β reconstitution in knockout mice accelerates healing but increases fibrosis. Moreover, the NLRP3 protein also modulates fibroblast phenotype independently of inflammasome activation via a ROS-dependent mechanism.

Conclusion: NLRP3 exerts dual-phase regulatory roles in wound healing: (i) during inflammation, it drives chemokine-mediated macrophage/fibroblast recruitment and M1 polarization while suppressing fibroblast-mediated repair via IL-1β signaling; (ii) later, NLRP3 deficiency enhances Wnt/Notch signaling, promoting structural restoration despite transiently delayed healing. Moreover, fibroblasts with high NLRP3 expression engage an inflammasome-independent NLRP3/ROS axis that augments activation of TGF-β/Smad signaling. These findings position NLRP3 as a potential therapeutic target for modulating phase-specific inflammatory and regenerative responses.

Received: 18 May 2025. **Revised:** 25 November 2025. **Accepted:** 3 January 2026
© The Author(s) 2026. Published by Oxford University Press.
This is an Open Access article distributed under the terms of the Creative Commons Attribution-NonCommercial License (https://creativecommons.org/licenses/by-nc/4.0/), which permits non-commercial re-use, distribution, and reproduction in any medium, provided the original work is properly cited. For commercial re-use, please contact reprints@oup.com for reprints and translation rights for reprints. All other permissions can be obtained through our RightsLink service via the Permissions link on the article page on our site—for further information please contact journals.permissions@oup.com.

Downloaded from academic.oup.com/burnstrauma/article/doi/10.1093/burnst/tkag002/8415534 by guest on 12 October 2026

Graphical abstract



Keywords NLRP3 inflammasome, Wound healing, Spatiotemporal regulation, Chemotaxis, Macrophage polarization, Fibroblast

Highlights

- **NLRP3 drives chemokine-dependent macrophage/fibroblast recruitment and M1 polarization during the inflammatory phase, while its deficiency enhances Wnt/Notch-mediated structural restoration during the proliferative phase, revealing phase-specific therapeutic potential.**
- **NLRP3 ablation rewires macrophage dynamics by suppressing M1 pro-inflammatory phenotypes and enhancing M2 reparative polarization, reshaping the immune microenvironment across healing phases.**
- **Macrophage NLRP3 inflammasome activation suppresses the pro-reparative phenotype and promotes a pro-inflammatory phenotype in fibroblasts via IL-1β. Conversely, inflammatory fibroblasts highly express NLRP3, which, independent of inflammasome assembly, amplifies TGF-β-induced Smad signaling through the NLRP3/ROS axis.**

Background

Wound healing is a meticulously orchestrated biological process characterized by sequential yet overlapping phases: hemostasis, inflammation, proliferation, and remodeling [1, 2]. Among these stages, the inflammatory response serves as a critical coordinator of cellular and molecular events essential for tissue repair. While transient inflammation clears pathogens and cellular debris, dysregulation—particularly excessive or prolonged activation—can lead to chronic wounds, fibrosis, and impaired regeneration [3, 4]. This delicate balance underscores the need to elucidate mechanisms that fine-tune inflammatory signaling to optimize the healing process.

Inflammasomes, particularly the NOD-like receptor family pyrin domain-containing 3 (NLRP3) inflammasome, have emerged as pivotal players in innate immunity and tissue repair [5, 6]. NLRP3 activation is triggered by both exogenous pathogen-associated molecular patterns (PAMPs) and endogenous damage-associated molecular patterns (DAMPs) released during injury and infection. The canonical activation pathway involves a two-step process: (i) priming via NF-κB signaling (e.g. triggered by TLR activation in response to DAMPs), which upregulates NLRP3 and pro-IL-1β expression, and (ii) activation by stimuli such as ATP or crystalline structures, leading to inflammasome assembly, caspase-1-mediated maturation of IL-1β and IL-18, and pyroptosis [6, 7]. While NLRP3 activation is indispensable for acute wound repair, its persistent activity drives chronic inflammation and fibrosis, as seen in diabetic ulcers and pathological scars [5, 8–10]. Despite its therapeutic potential, the spatiotemporal dynamics of NLRP3—how it temporally regulates interactions between immune cells (e.g. macrophages) and stromal cells (e.g. fibroblasts)—remain poorly defined, hindering targeted interventions.

Current studies predominantly focus on NLRP3's role in isolated cell types or phases. For example, NLRP3 in macrophages promotes IL-1β release to recruit neutrophils, while in fibroblasts, it may modulate extracellular matrix (ECM) remodeling [10–12]. However, wound healing necessitates dynamic crosstalk across phases: macrophages recruit fibroblasts via chemokines during early inflammation, while fibroblasts later transition to myofibroblasts to drive contraction and ECM deposition [13, 14]. Emerging evidence suggests NLRP3 orchestrates these interactions through IL-1β signaling, yet conflicting reports highlight a paradox—NLRP3 deficiency delays acute wound closure but reduces fibrosis [8, 10]. This apparent contradiction implies phase-specific roles: early activation to initiate repair versus later suppression to prevent pathological remodeling. Resolving this duality requires a systems-level approach to map NLRP3's spatiotemporal activity and its downstream cellular networks.

During cutaneous wound healing, precisely orchestrated chemotaxis sequentially recruits neutrophils, macrophages, fibroblasts, endothelial, and keratinocyte populations to the injury site [14–16]; however, the upstream molecular switches translating tissue damage into these chemotactic cues remain elusive. The NLRP3 inflammasome is a sentinel for both DAMPs and PAMPs that amplifies local innate immunity [6, 7].

Downloaded from academic.oup.com/burnstrauma/article/doi/10.1093/burnst/tkag002/8415534 by guest on 12 October 2026

Nevertheless, whether NLRP3 activation governs the spatiotemporal release of chemotactic gradients or directly dictates the migratory competence of repair-associated cells is still unknown. Elucidating this regulatory axis is critical to understand—and ultimately correct—chemotactic failure in chronic or infected wounds.

Here, we employed CRISPR/Cas9-generated Nlrp3−/− mice, multi-omics and functional assays to dissect NLRP3's roles across wound healing phases. We demonstrate that NLRP3 activation during inflammation drives macrophage-fibroblast recruitment via CCL/CXCL chemokines, while its suppression in later phases facilitates M2 macrophage polarization and tissue repair. Mechanistically, NLRP3 governs fibroblast phenotypic plasticity through L-1β-dependent macrophage to fibroblast crosstalk, linking inflammation to ECM remodeling. Notably, we corroborated these dynamics in human wounds, revealing conserved NLRP3 functions. Our findings redefine NLRP3 as a temporal gatekeeper of healing, offering a roadmap for phase-specific therapies to treat chronic wounds and fibrosis.

Materials and methods

Animals and model

All animal experiments were conducted in accordance with the guidelines of and approved by the Animal Ethics Committee of the Chinese PLA General Hospital (approval no. S2024-407-01). Wild-type (WT; C57BL/6 J) and Nlrp3−/− (C57BL/6 J background) mice were obtained from the Guangdong Cardiovascular Institute and housed in Shanghai Model Organisms Center under standard housing conditions. Genotyping identified homozygous Nlrp3−/− mice, which, along with WT littermates were used for subsequent experiments. Genotyping of mice was performed by PCR and agarose gel electrophoresis (Figure S1). All following experimental mice were 6–8 week-old and weighed 25–30 g, ensuring uniformity in age and growth phase.

WT and Nlrp3−/− mice full-thickness skin wound model

A full-thickness skin wound model was established as previously described [17]. Briefly, C57BL/6 J and Nlrp3−/− mice ($n = 20$ per group, with 4 mice per time point at days 0, 2, 4, 7, and 14 for subsequent tissue collection and analysis) were anesthetized with 1.5%–3% isoflurane in oxygen. After shaving the dorsal hair, a midline mark was made on the back, and the skin was disinfected. Using an 8 mm punch biopsy tool, a full-thickness skin wound was created at the marked site, and Tegaderm (3 M, USA) was used to cover the wound to prevent contamination.

IL-1β blockade in C57BL/6 J mice

To maximize biological replication while adhering to the 3Rs principle, two full-thickness excisional wounds (8 mm diameter) were created with a sterile disposable punch on the shaved dorsum of each C57BL/6 J mouse after isoflurane anesthesia. Consequently, total of 15 mice per group with three mice per time-point provided six identical wounds for statistical comparison. To neutralize endogenous IL-1β during healing, 50 μl containing 20 μg of either control IgG or anti-IL-1β neutralizing antibody (BE0246, BE0091, Invivomab) was administered subcutaneously at four equidistant points around each wound immediately after wounding and repeated on days 1, 3, and 5.

IL-1β supplementation in Nlrp3−/− mice

To restore the physiological IL-1β profile absent in Nlrp3−/− mice, recombinant murine IL-1β (R&D Systems) was injected subcutaneously in a volume of 50 μl according to the following schedule that mimics the natural temporal expression: 2 μg at Day 0, 10 μg at Days 1 and 3, and 2 μg at Day 5. Vehicle controls received an equivalent volume of PBS at identical time-points.

Wound healing was monitored and photographed on Days 0, 2, 4, 7, 10, and 14. Wound size was measured using ImageJ software, and wound healing progression was tracked. Tissue samples were divided into three groups: one for RNA sequencing, one for Western blotting (WB) and PCR analysis, and one for histological staining.

Murine bone marrow-derived macrophage and fibroblast isolation, cell culture, and treatment

Bone marrow-derived macrophages (BMDMs) were isolated from 8-week-old male Nlrp3−/− mice and their age-matched WT controls. Mice were euthanized by cervical dislocation, and the tibias and femurs were carefully dissected. Bone marrow was flushed from the cavities of the long bones using high-glucose Dulbecco's Modified Eagle Medium (DMEM, Biological Industries, Israel) with a 1 ml syringe. The cell suspension was then filtered through a 100 μm mesh and centrifuged at 1300 rpm for 5 min. The cell pellet was treated with red blood cell lysis buffer (eBioscience) for 3 min, followed by centrifugation and resuspension with culture medium. The cells were cultured in DMEM supplemented with 1% L-glutamine, 30 mM glucose, 10% fetal bovine serum (FBS, Gibco, USA), 1% penicillin–streptomycin (Solarbio, China), and 50 ng/ml Macrophage colony-stimulating factor (PeproTech). On Day 3, half of the culture medium was replaced, and on Day 5, the entire medium was refreshed. BMDMs were harvested on Day 7 for subsequent experiments. To induce polarization, BMDMs were stimulated with 1 μg/ml lipopolysaccharide (LPS, Sigma-Aldrich, USA) for 24 h to promote M1 polarization, or with 20 ng/ml IL-4 (Novoprotein, China) for 48 h to induce M2 polarization.

Primary fibroblasts were isolated from Neonatal Nlrp3−/− and WT mice. The neonatal mice were euthanized, and their skin was disinfected by immersion in 75% ethanol for 5 min. The full-thickness skin was then excised and placed epidermis side up in a sterile petri dish. After removing the epidermis using Dispase II (Roche, 2 mg/ml) overnight at 4°C, the dermal tissue was minced and placed in a centrifuge tube. The tissue was digested in 0.25% type I collagenase (ThermoFisher) for 30 min at 37°C. The cell suspension was filtered through a 100 μm cell filter and centrifuged to collect the fibroblast pellet. The isolated primary fibroblasts were cultured in DMEM supplemented with 30 mM glucose, 10% FBS, and 1% penicillin–streptomycin. Fibroblasts before passage 3 were used for further experiments. All cell cultures were maintained at 37°C in a 5% CO_2 incubator.

Downloaded from academic.oup.com/burnstrauma/article/doi/10.1093/burnst/tkag002/8415534 by guest on 12 October 2026

Coculture model

The transwell coculture system was used to assess the chemotactic effects of macrophages on fibroblasts. 50 000 J774.1 macrophage cells line were seeded in the lower chamber of a 24-well Transwell plate. After 24 h of incubation in complete DMEM supplemented with 10% FBS and 1% penicillin–streptomycin, the macrophages were stimulated under the following conditions: (i) macrophage (control group); (ii) macrophage + LPS: stimulated with 250 ng/ml LPS for 6 h; (iii) macrophage + LPS-ATP: stimulated with 250 ng/ml LPS for 5 h followed by the addition of 2 mM ATP (MCE, USA) and further incubation for 1 h; (iv) macrophage + MCC950 (MCE, USA): pretreated with 10 μM MCC950 for 2 h before LPS or ATP stimulation, followed by a 6-h treatment; (v) macrophage + LPS-ATP + MCC950: pretreated with 10 μM MCC950 for 2 h, followed by LPS stimulation for 5 h, and the addition of 2 mM ATP for 1 h. Following stimulation, the original medium was discarded, and fresh DMEM medium with 10% FBS was added to the macrophages. WT fibroblasts were then digested and seeded in the upper chamber, with serum-free DMEM placed in the lower chamber. After 24 h of coculture, cells were subjected to 0.3% crystal violet staining and photographed to evaluate fibroblast migration.

To evaluate the directional migration of THP-1–derived macrophages, a 24-well transwell system with 8-μm pore polycarbonate membranes (Corning) was used. 100 000 THP-1 cells in 200 μl RPMI-1640 containing 10% FBS were seeded into the upper chambers. The lower chambers contained 600 μl of the same medium supplemented with 100 ng ml^{-1} PMA to induce M0 macrophage differentiation. After 24 h, non-adherent cells were removed, and adherent macrophages were exposed to the same treatments as J774.1 cells in fresh RPMI-1640 containing 2% FBS. Cells were allowed to migrate for an additional 24 h in serum-free RPMI-1640. Non-migrated cells on the upper surface were gently removed with cotton swabs, whereas migrated cells on the lower surface were fixed with 4% paraformaldehyde for 15 min, stained with 0.3% crystal violet for 15 min, and washed three times with PBS. Images were captured under a light microscope at 200× magnification, and cells in five random fields per insert were counted.

For fibroblast chemotaxis, 10 000 human skin fibroblas (HSFs) in 200 μl serum-free DMEM were seeded into the upper chambers. THP-1–derived macrophages in the lower chambers were exposed to the same treatments as J774.1 cells to serve as a chemoattractant. Cells were allowed to migrate for an additional 24 h in serum-free RPMI-1640, and crystal violet staining and photographed were used to evaluate fibroblast migration.

To further investigate the influence of NLRP3 inflammasome activation in macrophages on fibroblasts, an fibroblast coculture model was used. After macrophage stimulation with 250 ng/ml LPS for 5 h, followed by 1 h 2 mM ATP treatment, the conditioned medium (CM) was collected. The medium was used to treat both WT and KO fibroblasts for 24 h. Following treatment, cells were harvested for further analysis.

Histological, immunohistochemistry, and immunofluorescence staining

At the designated time points, dorsal wound tissues were collected from anesthetized mice, fixed in 4% paraformaldehyde, decalcified, and embedded in paraffin using standard protocols. Hematoxylin and eosin (H&E, Beyotime, China) staining was performed to examine the anatomical structure of the wound and surrounding microvessels. Masson's trichrome staining (M&T, Solarbio, China) was used to assess the wound area, including the hair follicle structure and collagen deposition within the wound bed.

For immunohistochemistry staining (Beyotime, China), tissue sections were permeabilized with 0.3% Triton X-100 for 10 min at room temperature, followed by blocking with 10% goat serum and 3% hydrogen peroxide in PBS. The sections were then incubated overnight at 4°C with the appropriate primary antibodies. IHC staining was performed using horseradish peroxidase (HRP)-conjugated secondary antibodies, with 3,3′-diaminobenzidine (DAB) used for visualization.

For cell immunofluorescence staining (IF), BMDMs or fibroblasts were cultured in 35 mm confocal dishes and stimulated with the specified reagents. The cells were washed with PBS, fixed in 4% paraformaldehyde for 15 min, and permeabilized with 0.3% Triton X-100 for 20 min at room temperature. After washing three times with PBS, the cells were blocked with 10% normal goat serum (Solarbio, China) for 1 h and incubated overnight at 4°C with the primary antibodies. The cells were then incubated with the appropriate fluorescently labeled secondary antibody at room temperature for 2 h in the dark. Confocal images were captured using a TCS SP8 confocal microscope (Leica, Germany). Image analysis was performed using ImageJ software. For IF staining of tissue sections, the slides were deparaffinized and subjected to antigen retrieval. The subsequent steps followed the same procedure as for the cell IF staining. The primary and secondary antibodies used for IHC and IF are detailed in Table S1.

Western blot

At the designated time points, protein samples were collected by lysing cells or tissues using sodium dodecyl sulfate (SDS) lysis buffer supplemented with protease inhibitors (Roche). The protein extracts were then separated by 10% SDS-polyacrylamide gel electrophoresis and transferred onto a methanol-activated polyvinylidene difluoride (PVDF) membrane (GE Healthcare, USA). Following the transfer, the membrane was incubated with TBST buffer containing 5% bovine serum albumin (BSA) to block non-specific binding sites. The membrane was then probed overnight at 4°C with an anti-NLRP3 antibody (1:1000, AG-20B-0014-C100, AdipoGen Life Sciences). As a loading control, the membrane was incubated with anti-GAPDH antibody (1:5000, 60–004–1-Ig, Proteintech, USA). Protein expression levels were detected using an enhanced chemiluminescence system (Applygen, China) and visualized with a UVITEC Alliance MINI HD9 imaging system (UVITEC, UK). The other primary antibodies used for WB are detailed in Table S1.

Ribonucleic acid extraction and reverse transcription quantitative polymerase chain reaction

Tissue or cell samples were homogenized and lysed in Trizol reagent (Ambion, USA) to extract total RNA. The cDNA was synthesized from RNA using the PrimeScript RT Reagent Kit with gDNA Eraser (Takara, China) following the manufacturer's

Downloaded from academic.oup.com/burnstrauma/article/doi/10.1093/burnst/tkag002/8415534 by guest on 12 October 2026

reverse transcription protocol. Quantitative real-time PCR (RT-qPCR) was performed using TB Green Premix Ex Taq II (Takara, China) on a QuantStudio 5 system (Applied Biosystems, USA). The relative expression levels of target genes were calculated using the $2-\Delta\Delta$Ct method, with glyceraldehyde-3-phosphate dehydrogenase (Gapdh) as the reference gene. The primers for the target genes are provided in Table S2.

Flow cytometry assay

Single-cell suspensions were prepared from wound tissues of WT and Nlrp3−/− mice at Day 2 post-wounding. Tissues were dissociated using an enzymatic cocktail containing 1 mg/ml Liberase TM (900 μl; Roche, USA), 1 mg/ml DNase I (150 μl; Roche, USA), and 950 μl RPMI-1640 medium. The resulting cell suspensions were harvested, washed twice with PBS, and subsequently stained for surface markers using antibodies against CD11B, F4/80, and CD86 (all from BD Biosciences, USA). Staining was performed for 1 h at 4°C in the dark. For the polarization assay, BMDMs from WT and KO mice were treated with 20 ng/ml IL-4 for 48 h to induce M2 polarization, followed by staining with antibodies against CD11B and CD206 (BD Biosciences, USA).

Flow cytometry was performed on a BD flow cytometer (BD Biosciences, USA). A standardized gating strategy was applied to all samples: single cells were first gated based on FSC-A/SSC-A profiles, followed by FSC-H/FSC-A to exclude doublets. From the singlet population, CD11b-positive cells were selected, and macrophages were further identified as F4/80high cells within the CD11b+ gate. Macrophage subsets were defined as CD86high for M1-like or CD206high for M2-like phenotypes, with the positivity thresholds established using negative controls. Unstained samples and single-stain controls were included for each experimental group and genotype to optimize instrument voltage settings and calculate compensation matrices. Detailed antibody information is provided in Table S1.

To evaluate the differential production of reactive oxygen species (ROS) by WT and Nlrp3−/− fibroblasts, cells were plated at a density of $2 \times 10\hat{}5$ per well in 12-well plates and grown to 80% confluence in complete DMEM. The culture medium was then replaced with fresh DMEM containing 2% FBS, and the cells were subjected to one of the following treatments: (1) IL-1β (10 ng/ml); (2) TGF-β (20 ng/ml); (3) IL-1β (10 ng/ml) + TGF-β (20 ng/ml); (4) LPS (500 ng/ml) for 4.5 h; or (5) LPS (500 ng/ml) for 4.5 h followed by ATP (2 mM) for 1 h. After stimulation, adherent cells were gently detached with Accutase (Sigma), washed once in PBS, and incubated with 5 μM dihydroethidium (DHE, Beyotime, China) in 600 μl PBS at 37°C for 30 min in the dark. Cells were then washed once in PBS, resuspended in 500 μl PBS, and immediately analyzed on a flow cytometer (BD Biosciences, USA). A minimum of 10 000 events per sample were acquired; the median fluorescence intensity (MFI) of the PE channel was used as a quantitative index of intracellular ROS. Data were analyzed using FlowJo v10.8.1.

CCK-8 and scratch assay

Cell proliferation of fibroblasts was assessed using the CCK-8 assay kit (Dojindo, Japan) according to the manufacturer's instructions. Cells were treated under different conditions, including the co-culture setup, and proliferation was measured at specified time points by adding CCK-8 reagent and measuring absorbance at 450 nm.

For the scratch migration assay, cells were treated with various interventions, and once the cells reached 90% confluence, a scratch was created using a 200 μl pipette tip. The pipette tip was gently used to create a consistent scratch perpendicular to the marked line. After scratching, the cells were washed twice with PBS to remove any detached cells. Fresh medium containing 1% FBS was added, and images were captured at the marked line under a microscope. The scratch area was monitored and photographed every 24 h at the same location. The images collected at different time points were analyzed using ImageJ software to quantify the cell migration.

RNA sequencing and data analysis

Tissue mRNA was extracted from tissue samples using the fixed and recovered intact RNA protocol. Wound tissue samples were processed for sequencing using the Illumina NovaSeq™ 6000 platform (LC Sciences). Differentially expressed genes (DEGs) were identified by applying a false discovery rate (FDR) threshold of <0.05 and an absolute fold change ≥ 1. These DEGs were further subjected to the Gene Ontology (GO) function and KEGG pathway enrichment analysis using the DAVID bioinformatics resources (https://davidbioinformatics.nih.gov/). The results of GO and KEGG enrichment analyses were visualized using an online platform (https://www.bioinformatics.com.cn, accessed on 10 December 2024) for data analysis and visualization.

For mouse wound analysis, the microarray dataset GSE23006 was downloaded from the GEO public database (https://www.ncbi.nlm.nih.gov/geo/query/acc.cgi?acc=GSE23006). This dataset includes gene expression data from mouse full-thickness wounds (1 mm) at various time points (0 h, 6 h, 12 h, 24 h, 3d, 5d, 7d, 10d), with three samples per time point. Differential gene expression analysis was conducted using the limma package in R (version 4.3.3), where all eight time points were compared in pairwise combinations, resulting in 28 comparisons. DEGs were identified with the criteria of $|\log2 \text{ fold change (FC)}| > 1$ and $P < 0.05$. The intersection of all DEGs was used to identify genes closely associated with wound healing. For functional analysis, the identified DEGs were submitted to the DAVID online tool for GO and KEGG pathway enrichment analysis. The GO terms included biological process, cellular component, and molecular function. To analyze the temporal expression patterns of these genes, we employed the Mfuzz package (version 2.62.0) for time-series clustering, setting the number of clusters to 10. GO and KEGG pathway analyses were then conducted for cluster 1, which primarily consisted of inflammation-related genes.

For the analysis of human wound data, the RNA sequencing dataset GSE174661 was downloaded from the GEO public database (https://www.ncbi.nlm.nih.gov/geo/query/acc.cgi?acc=GSE174661). This dataset encompasses gene expression data from acute human wounds at distinct time points (0 day, 1 day, and 7 day), with 5 samples per time point, as well as 5 cases of venous ulcer. Based on the sample correlation principal component analysis (PCA) clustering, 4 samples were selected from each group for subsequent analysis. The FPKM values of the sample expression were normalized according to gene expression levels, and the expression levels of NLRP3 in each

Downloaded from academic.oup.com/burnstrauma/article/doi/10.1093/burnst/tkag002/8415534 by guest on 12 October 2026

group were extracted for comparison. Furthermore, GSEA analysis was performed between each pair of groups to compare the differentially expressed related pathways.

Single-cell RNA sequencing data analysis of mouse acute wound

The scRNA-seq data used in this study were downloaded from the Genome Sequence Archive (GSA: CRA010641) at the China National Center for Bioinformation. For this analysis, we focused on four specific subsets related to the normal wound healing process: skin_YD0, skin_YD2, skin_YD4, and skin_YD7. Downstream analyses were performed using the Seurat software package (version 5.0.3), which included quality control, data integration, cell type identification, and differential gene expression analysis. Cells were filtered based on the following criteria: number of detected genes: $500 < \text{nFeature_RNA} < 7000$; percentage of mitochondrial gene expression: mt_percent $<20\%$; percentage of hemoglobin gene expression: HB_percent $<5\%$; Total RNA counts: $1000 < \text{nCount_RNA} <$ 97th percentile. To address potential batch effects from biological replicates within each group, the Harmony package was employed for data integration. After integration, the data were scaled using the ScaleData function. PCA was performed with the RunPCA function, retaining the first 30 principal components (dims = 1:30) for subsequent analysis. Unsupervised clustering was conducted using the FindNeighbors and FindClusters functions, with a resolution parameter set to 0.3. To identify marker genes specific to each cluster, the FindAllMarkers function was used with thresholds of an average log2 fold change (avg_log2FC > 0.25) and an adjusted p-value (p_val_adj < 0.05). These marker genes were then used to assign cell types to the clusters based on known gene expression patterns.

Cell–cell communication across different cell types was analyzed using the CellChat R package (version 1.6.1). This package infers interactions based on ligand-receptor pairs from the CellChatDB database. The CommunProbPathway function was employed to infer cell–cell communication at the signaling pathway level. The communication probabilities were calculated by summing the probabilities of related ligand-receptor pairs, thereby quantifying the strength of the interactions.

Pseudotime analysis, trajectory construction, and calculation of pseudotime-dependent gene expression were performed using the Monocle2 package (version 2.24) in R. After integrating the fibroblast subset into the Seurat object, the data were converted into a Monocle-compatible Cell Dataset. The analysis followed the recommended pipeline. Genes with expression >0.1 and expressed in at least 10 cells were retained for subsequent analysis. Size factors and dispersions were estimated, and t-SNE reduction and clustering were performed. For pseudotime ordering, the DispersionTable function was used to calculate gene expression dispersion, selecting genes with expression ≥ 0.1 and a dispersion greater than or equal to the fitted dispersion. These high-variance genes were used for pseudotime analysis, and trajectories were constructed using DDRTree. Differential gene analysis of the differentiation process (states) was performed with the differential GeneTest function. The top 20 DEGs related to differentiation were selected, and pseudotime-dependent gene expression was visualized using the plot_pseudotime_heatmap function from the viridis (version 0.6.5) package.

Single-cell RNA sequencing data analysis of human acute wound

The single-cell RNA sequencing (scRNA-seq) data of human wounds utilized in this study were downloaded from the GSE241132 dataset. This dataset comprises 12 samples from 4 time points, namely the skin tissue wounds of 3 healthy donors at Day 0, Day 1, Day 7, and Day 30, with biopsies taken from the same site. The human single-cell data were processed following a protocol analogous to that employed for mouse data. For this analysis, we conducted data quality control and integration based on the code and parameters provided in the previous original article. In total, 58 814 cells and 22 139 genes from 12 samples of acute wounds were retained for downstream analysis. Uniform Manifold Approximation and Projection (UMAP) and k-nearest neighbors graph were generated using the RunUMAP and FindNeighbors functions in Seurat (version 5), respectively. Major cell clusters were identified using the Louvain graph-based algorithm with a resolution of 0.5, resulting in 27 clusters. Subpopulation analyses of macrophages were performed using the same pipeline as for major cluster identification, which included normalization, variable feature selection, batch correction, dimensionality reduction, and unsupervised clustering, but with a resolution of 0.2.

Wound-tissue IL-1β quantification by enzyme-linked immunosorbent assay

On post-wounding days 2 and 4, the entire 8-mm wound area (including 2 mm of adjacent unwounded margin) was excised from each mouse, snap-frozen in liquid nitrogen, and stored at $-80°C$ until processing. Tissues were homogenized in ice-cold RIPA buffer (Beyotime, China) supplemented with 1 mM PMSF and $1\times$ protease inhibitor cocktail (Roche) using a bead-beater (25 Hz, 60 s). Homogenates were centrifuged at 12000 $\times$ g for 15 min at $4°C$, and supernatants were assayed for IL-1β concentration with a commercially available mouse IL-1β ELISA kit (BY-EM220174, Byabscience, China) according to the manufacturer's protocol. Total protein content was determined by BCA assay (Solarbio Life Sciences) to normalize cytokine levels. Data are expressed as pg IL-1β per mg total protein.

Statistical analysis

All experiments were performed with at least three replicates, and the sample sizes are indicated in the figure legends. Results are expressed as the mean $\pm$ standard deviation (SD). Statistical analyses were conducted using GraphPad Prism 9.5.0 (GraphPad, USA). Post-hoc power analysis was performed using G*Power software (version 3.1.9.7) for the primary outcome measure of wound closure rate at Day 4. Comparisons between two groups were performed using an unpaired two-tailed t-test, while comparisons among multiple groups were conducted using one-way or two-way analysis of variance (ANOVA), followed by Tukey's multiple

Downloaded from academic.oup.com/burnstrauma/article/doi/10.1093/burnst/tkag002/8415534 by guest on 12 October 2026

comparisons test. A P-value of <0.05 was used a statistical significance threshold. The significance levels are denoted as $^{*}P<0.05$, $^{**}P<0.01$, $^{***}P<0.001$, and $^{****}P<0.0001$.

Results

NOD-, LRR- and pyrin domain-containing protein 3 dynamic changes may participate in the regulation of the wound healing process

To gain insights into the molecular mechanisms governing wound healing, we conducted bioinformatics analysis of the GSE23006 microarray dataset, which encompasses the gene expression profiles of mouse skin wounds from Day 0 to Day 10, spanning the entire wound healing process [18]. To identify key genes involved in the wound healing process, we paired the eight time-point groups, creating 28 combinations. Subsequently, Differential expression analysis were performed on each combination, and the Union of all DEGs (total number: 2211) was taken for follow-up analysis (Figure 1a). To further verify the functions of these genes, we conducted GO analysis. The results showed that these genes are involved in almost all biological processes critical to wound healing, such as inflammatory response, immune system process, cell proliferation, angiogenesis, and epithelialization (Figure 1b). Significantly, emerging evidence highlights the indispensability of intricate intercellular crosstalk during the inflammatory phase for successful acute wound resolution [1, 8, 19, 20]. To further identify the key inflammatory and immune regulatory genes involved in acute wound healing, we performed Mfuzz time-series analysis clustering of all DEGs, yielding 10 distinct transcriptional modules. Based on previous studies of the expression patterns during the inflammatory phase [18, 20–22], we prioritized Cluster 1 as it represents a gene set crucial for regulating inflammation (Figure 1c). GO and KEGG enrichment analyses of cluster 1 confirmed significant enrichment in inflammatory and immune-related pathways, particularly the NOD-like receptor signaling pathway and the NF-κB pathway (Figure 1d).

Intriguingly, the NLRP3 inflammasome, a master regulator of innate immune activation and inflammatory responses, is closely linked to both the NOD-like receptor signaling pathway and the NF-κB pathway. Given its established role in cutaneous repair, we analyzed the gene expression dynamics of *Nlrp3* and *Il1b*, which initiate the NLRP3 inflammasome in two wound models, RNA-seq datasets of different sizes (1 mm and 8 mm) [17, 18]. The results demonstrated a significant upregulation of NLRP3 during the inflammatory phase, followed by a rapid downregulation, and restoration to baseline levels as the wound almost re-epithelialization (Figure 1e). With the increase in wound size and the extension of healing time, the time for *Nlrp3* and *Il1b* gene expression to return to normal is also prolonged. Moreover, strong positive correlations were observed between *Nlrp3* expression and critical healing regulators (e.g. *Il1β*, *Tgfβ1*, *Mmp9*; Figure 1f). Collectively, these findings suggest that the dynamic activation of the NLRP3 inflammasome may be involved in regulating the wound healing process.

Deletion of NOD-, LRR- and pyrin domain-containing protein 3 delays dorsal skin wound healing in mice but improves wound healing quality

NLRP3 is critical for inflammasome assembly and activation [7]. To investigate its role in wound healing, we utilized CRISPR-Cas9-generated Nlrp3 KO mice and created a full-thickness skin injury model (Figure 2a). Our results demonstrated that Nlrp3 gene and protein expression levels were significantly elevated during the early inflammatory phase in WT wounds but gradually decreased over time. In contrast, expression levels remained negligible in uninjured skin and Nlrp3 KO mice (Figure 2b and c). Analysis of wound healing speed showed significantly delayed healing in Nlrp3 KO mice compared to WT mice at days 2,4,7 after skin injury, especially on the 2nd and 4th days (Figure 2d and e). Interestingly, Day 7 post-injury displayed a marked increase in collagen in KO wounds relative to WT wounds. However, by Day 14, collagen deposition in KO wounds was on par with WT wounds (Figure 2f–h). Additionally, KO wounds exhibited enhanced hair follicular formation at the wound margins compared to WT wounds on Day 14, and the epidermal thickness of KO wounds on days 7 and 14 post-injury was always lower than that of WT wounds and closer to that of normal skin (Figure 2g and h). These findings were further supported by IF staining, which revealed significantly higher expression of α-smooth muscle actin (α-SMA), collagen type I (COLI), collagen type III (COLIII), and TGF-β1 expression in KO wounds at Day 7, but relatively lower expression of COLI and TGF-β1 at Day 14 (Figure 2i and j). In summary, Nlrp3 deletion delays inflammatory-phase wound healing but displays higher-quality tissue repair characterized by reduced COLI and TGF-β1 expression and enhanced appendage restoration.

Spatiotemporal dynamics of the NOD-, LRR- and pyrin domain-containing protein 3 inflammasome during mouse wound healing

To explore the spatiotemporal distribution of NLRP3, we performed bioinformatic analysis on single-cell RNA sequencing data from a publicly available mouse full-thickness skin injury model [23]. Cell population dynamics mirrored classical wound healing phases: inflammatory cells, notably macrophages and neutrophils, dominated the early inflammatory phase (days 2–4 post-injury), while fibroblasts, epithelial cells, and endothelial cells prevailed during the repair phase (Day 7) (Figure 3a and b, and Figure S2a and b). *Nlrp3* and *Il1b* expression was enriched in macrophages and neutrophils, with lower expression levels observed in fibroblasts (Figure 3c–e). Notably, the proportion of NLRP3-positive cells and their average expression levels were positively correlated (Figure 3d and e and Figure S2c and d). NLRP3 exhibited dynamic expression patterns in macrophages and fibroblasts throughout the wound healing process, whereas neutrophils maintained persistently high expression. These results suggest that the dynamic expression of *Nlrp3* in macrophages

Downloaded from academic.oup.com/burnstrauma/article/doi/10.1093/burnst/tkag002/8415534 by guest on 12 October 2026

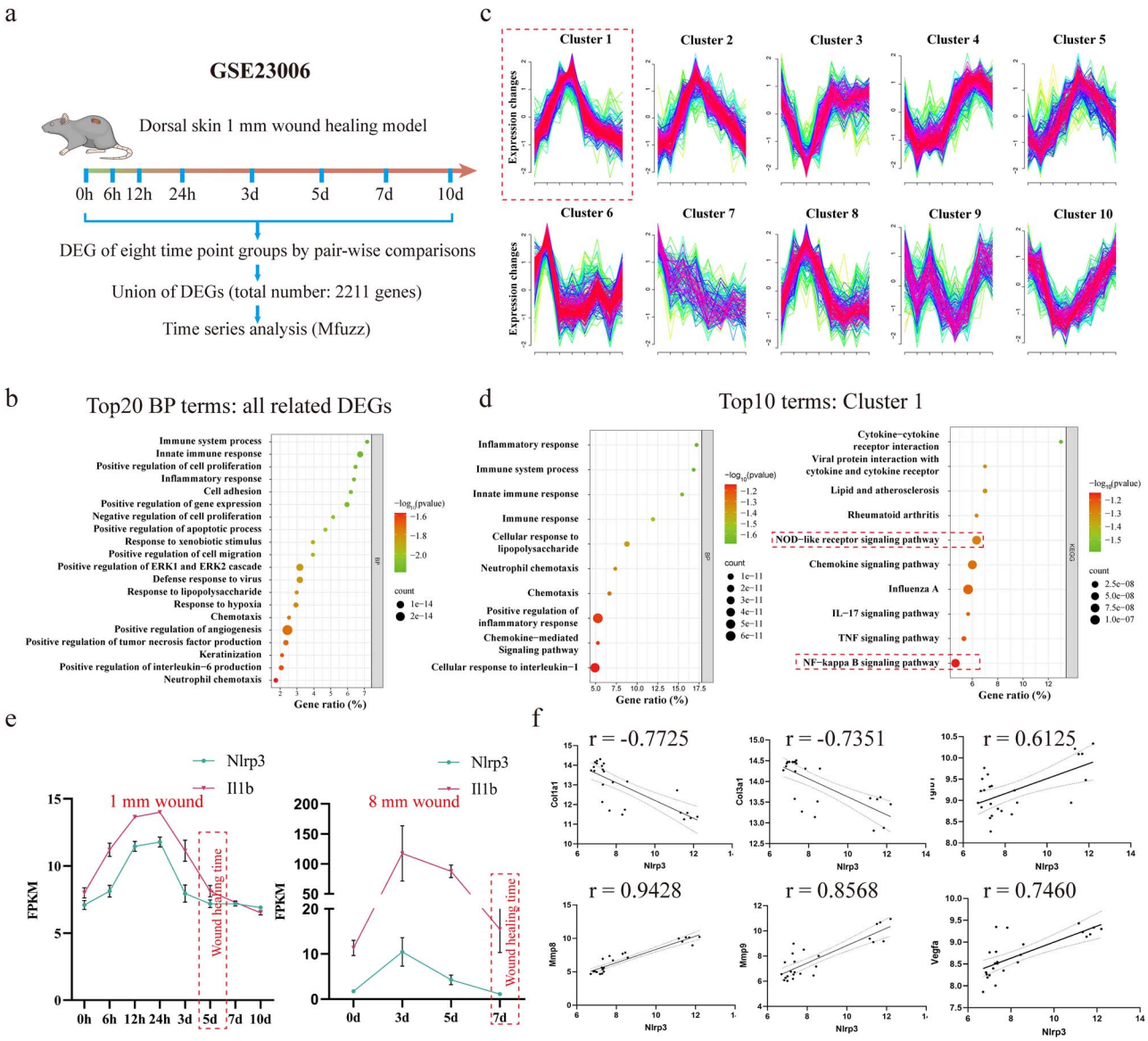


Figure 1 Microarray data GSE23006 reveal the correlation between NLRP3 inflammasome activation and wound healing. (**a**) Workflow diagram for GSE23006 microarray data analysis from the GEO database. (**b**) GO enrichment analysis of the top 20 biological processes terms associated with DEGs during wound healing. All related DEGs were from the union of DEGs from pairwise comparisons across all time points during wound healing. (**c**) Time-series analysis (Mfuzz) of all DEGs during wound healing. (**d**) GO enrichment analysis of the top 20 biological processes terms associated with cluster 1 from (c). (**e**) Transcriptomic analysis reveals dynamic expression of NLRP3 inflammasome prime related genes (*Nlrp3*, *Il1b*) during wound healing in different wound sizes. Left panel (GSE23006 dataset, 1 mm wound), right panel (8 mm full-thickness skin wound RNA-sequence data from our published paper [17]); wound healing time: red dashed box. (**f**) Correlation analysis between *Nlrp3* expression and wound healing-related genes (*Col1a1*, *Col3a1*, *Tgfb1*, *Mmp8*, *Mmp9*, and *Vegfa*) in the GSE23006 dataset. *GO* gene ontology, *BP* Biological process, *DEG* differentially expressed gene

and fibroblasts may play a more critical role in regulating wound healing. As NLRP3 is a key regulator of the IL-1 signaling pathway, we analyzed ligand-receptor interactions within this pathway. The results revealed high expression of *Il1b* ligands in macrophages and neutrophils, while receptors such as *Il1rap* were highly expressed in fibroblasts, neural cells, and epithelial cells. Additionally, fibroblasts, endothelial cells, hair follicle cells, and epithelial cells expressed high levels of *Il1r1*, *Il1rl1*, and *Il1rl2* receptors, indicating that macrophages and neutrophils may regulate fibroblast functions through IL-1 signaling during wound healing (Figure S2e).

IF co-localization further confirmed that NLRP3 was predominantly expressed in macrophages (F4/80+) and neutrophils (LY6G+) during the early inflammatory phase (Day 2) (Figure 3f). IHC revealed widespread activation of NLRP3 and IL-1β in the inflammatory phase (Day 2 and Day 4), which became relatively low expression and localized to the superficial dermis during the repair phase (Day 7) (Figure 3g and h). Collectively, these findings indicated that NLRP3 is mainly expressed in macrophages and neutrophils during wound healing, with low expression in fibroblasts. Its dynamic expression in macrophages and fibroblasts resembles the NLRP3 inflammasome activation pattern

Downloaded from academic.oup.com/burnstrauma/article/doi/10.1093/burnst/tkag002/8415534 by guest on 12 October 2026

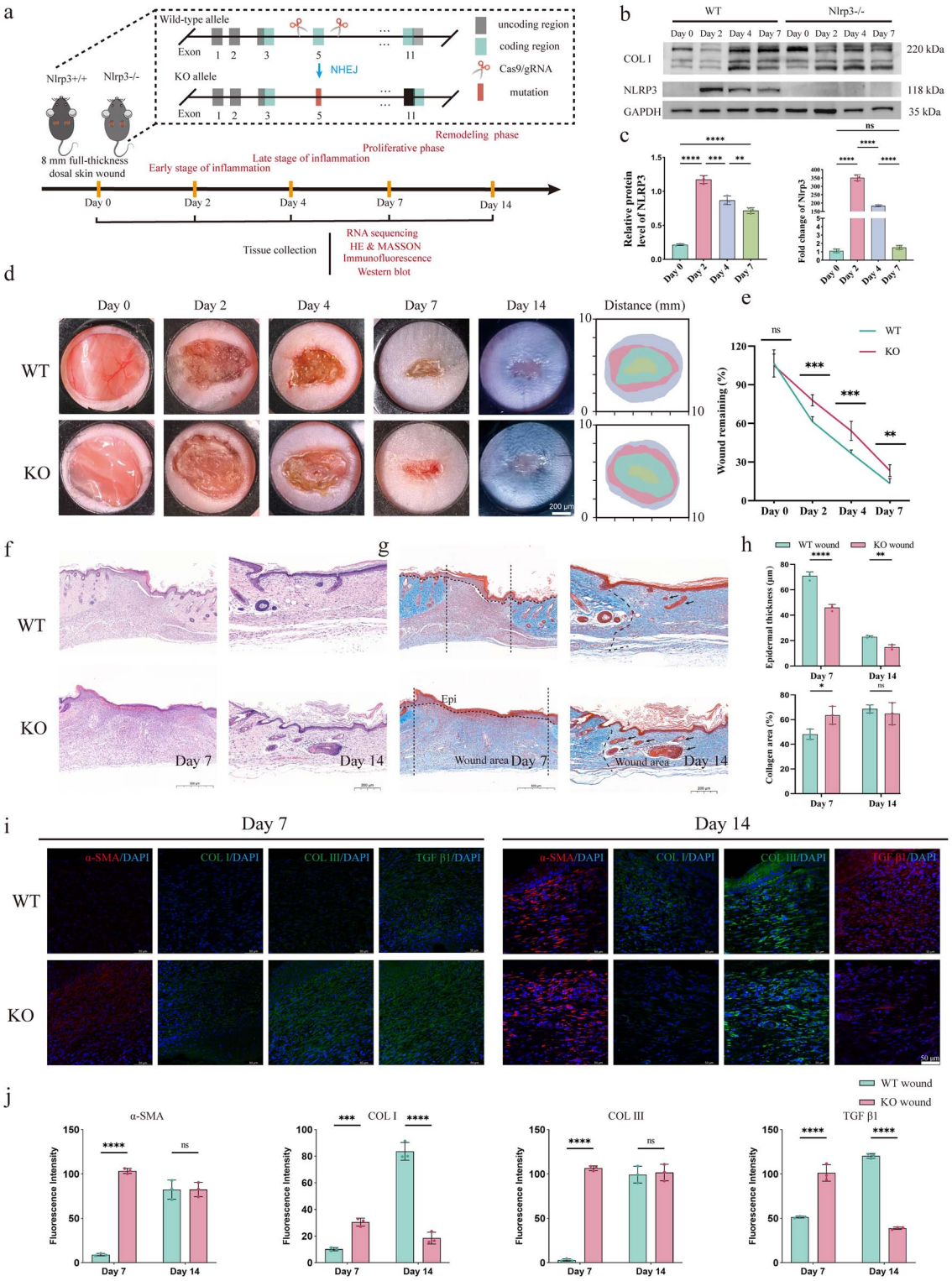


Figure 2 *In-vivo* experimental evaluation of the effects of NLRP3 KO on wound healing. (**a**) Strategy for generating Nlrp3 KO mice and schematic representation of the animal experiments. (**b**) Western blot analysis of NLRP3 and COL1 protein expression in WT and KO mice at various time points (Days 0, 2, 4, and 7) post-injury. GAPDH was used as a loading control. (**c**) Relative protein and mRNA expression of NLRP3 in WT mice at various time points (days 0, 2, 4, and 7) post-injury. Data of mRNA are presented as fold changes relative to Day 0 (mean ± SD, $n = 3$). (**d**) Representative optical images of wounds and wound area tracing analysis corresponding to optical images on days 0, 2, 4, 7, and 14. Scale bar, 200 μm. (**e**) Quantitative analysis of wound remaining ratio on Days 0, 2, 4, and 7 from (d). $n = 4$. (**f**) Representative H&E staining of wounds on Days 7 and 14. Scale bar, 500 and 200 μm. (**g**) Representative Masson trichrome staining of wounds on Days 7 and 14. Scale bar, 500 and 200 μm. Black dashed lines delineate the wound margin. The black arrow denotes hair follicles inside the wound. (**h**) The quantification analysis of collagen area and epidermal thickness in the wound from (g). (mean ± SD, $n = 3$). (**i**) Representative IF images of α-SMA (red), COLI (green), COLIII (green), and TGFβ1 (green for Day 7 and red for Day 14). Cell nuclei are counterstained with DAPI (blue). Scale bar, 50 μm. (**j**) Quantitative analysis of IF staining for α-SMA, COLI, COLIII, and TGF-β1 in the wound from (i) (mean ± SD, $n = 3$). WT, Nlrp3+/+: WT; KO, Nlrp3−/−: KO. *KO* NLRP3 knockout, *WT* wild-type

Downloaded from academic.oup.com/burnstrauma/article/doi/10.1093/burnst/tkag002/8415534 by guest on 12 October 2026

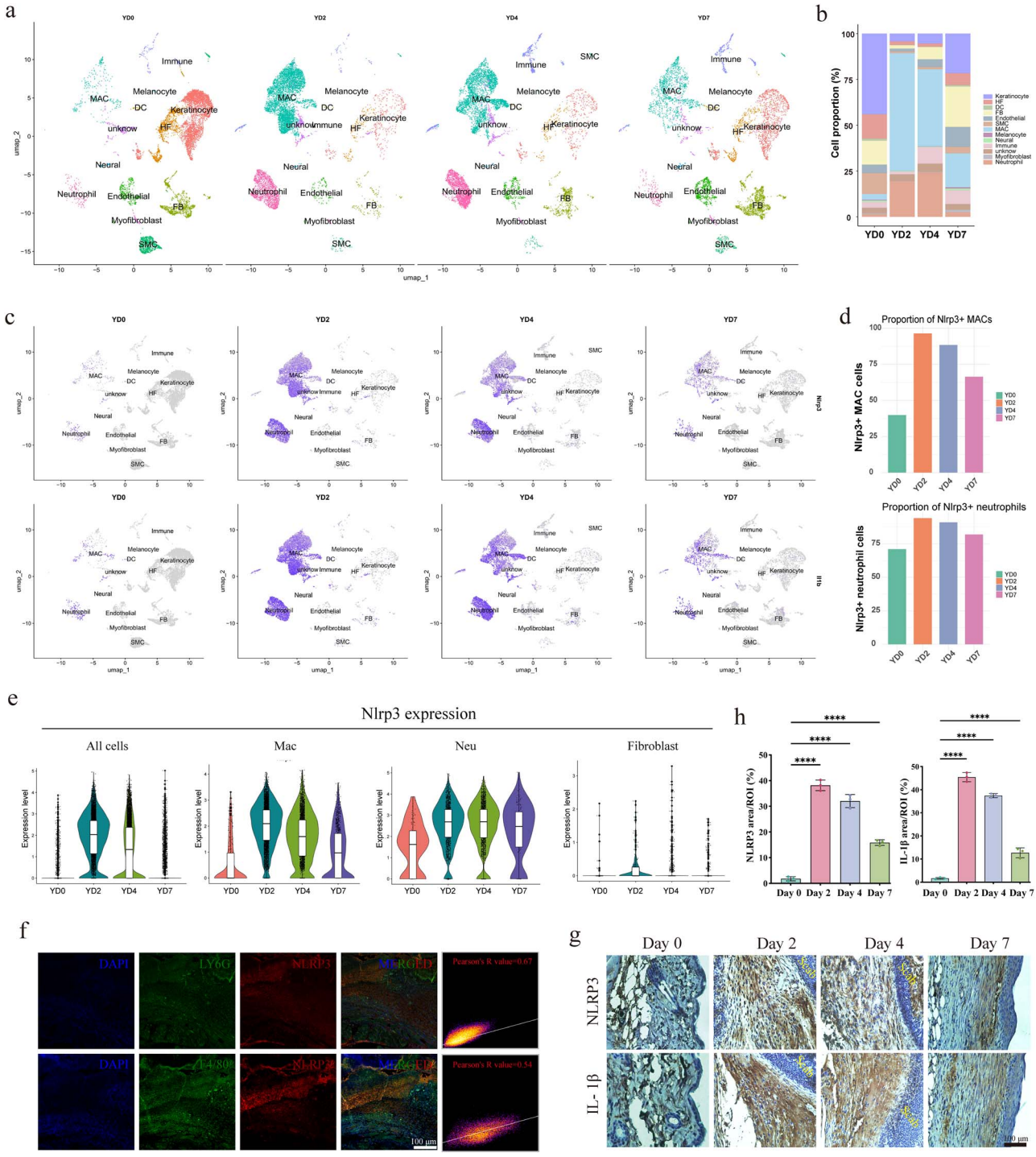


Figure 3 Spatiotemporal dynamics of the NLRP3 inflammasome during mouse wound healing. (**a**) UMAP plots of single-cell RNA sequencing reveal dynamic cellular compositions at different time points during wound healing. (**b**) Bar charts show the changes in the proportion of wound cells at different time points. (**c**) Spatiotemporal dynamic gene expression of *Nlrp3* and Il1b during wound healing. (**d**) Proportion changes of *Nlrp3*-positive macrophages and neutrophils during wound healing. (**e**) Average expression levels of *Nlrp3* across different cell types during wound healing. (**f**) IF colocalization of NLRP3 with LY6G and F4/80 on Day 2 post-wounding. NLRP3 (red), LY6G (green), F4/80 (green), and DAPI (blue). Scale bar, 100 μm. (**g**) Immunohistochemical analysis of NLRP3 and IL-1β expression during different phases of wound healing. Scale bar, 100 μm. (**h**) Quantitative analysis of NLRP3 and IL-1β expression in wound tissues during different phases of wound healing (mean $\pm$ SD, $n = 3$). Scale bar, 100 μm. *Neu* neutrophil, *SMC* smooth muscle cell, *HF* hair follicle, *UMAP* uniform manifold approximation and projection, *MAC* macrophage, *HF* hair follicle

Downloaded from academic.oup.com/burnstrauma/article/doi/10.1093/burnst/tkag002/8415534 by guest on 12 October 2026

during wound healing, suggesting these cells may be key regulators in NLRP3 inflammasome-mediated regulation of wound healing.

NOD-, LRR- and pyrin domain-containing protein 3 knockout impairs the chemotaxis of macrophages and fibroblasts to the wound during the inflammatory phase

To investigate the role of the NLRP3 inflammasome in early wound healing, RNA sequencing was performed on wound tissues from WT and Nlrp3 KO mice on Day 2 post-injury. Transcriptomic analysis identified 441 upregulated and 786 downregulated genes in Nlrp3 KO wounds compared to WT (Figure 4a). GO and KEGG pathway analyses revealed significant downregulation of inflammation response and immune system processes, including the NOD-like receptor signaling pathway, Toll-like receptor signaling pathway, and NF-κB signaling pathway (Figure 4b). Chemotaxis-related pathways, such as the chemokine signaling pathway and cytokine-cytokine receptor interaction, were also significantly downregulated (Figure 4b). Heatmap analysis highlighted reduced expression of key chemotactic mediators, including Ccl2, Ccl3, and Ccl7 in the CCL pathway, and Cxcl12 and Cxcr3 in the CXCL pathway (Figure 4c). These findings suggest that Nlrp3 deficiency may impair the recruitment of inflammatory and reparative cells to the wound site through CCL/CXCL pathways during the early phase of wound healing.

To further understand the impact of NLRP3 inflammasome activation on cell recruitment, we performed ligand-receptor expression and cell-communication analyses on single-cell sequencing data [23]. Prior studies demonstrated that NLRP3 activation peaks during the early inflammatory phase (Figures 1–3). Therefore, we focused on the significantly upregulated cellular communication on Day 2 post-injury. Ligand-receptor expression analysis showed that Ccl2, Ccl3, and Ccl7 were predominantly expressed in macrophages and fibroblasts on Day 2 post-injury, while Cxcl12 was enriched in fibroblasts (Figure S3a). Comparative analysis of uninjured and injured skin revealed that the CCL signaling pathway was markedly enhanced on Day 2, with macrophages acting as both signal senders and receivers. fibroblasts also exhibited upregulated CCL signaling and CXCL signaling as signal senders (Figure S3b). Notably, these chemokines were significantly downregulated in Nlrp3 KO mice (Figure 4c), suggesting that NLRP3 activation influences chemokine expression, thereby regulating immune and reparative cell recruitment, particularly macrophages and fibroblasts.

Further analysis of the interactions between macrophages and fibroblasts during the inflammatory phase revealed that macrophages can influence fibroblast function via chemokine-related ligand-receptor interactions and IL-1 signaling pathway ligand-receptor interactions in the early inflammatory phase (Day 2) (Figure S3c). Moreover, fibroblasts can influence macrophage function via chemokine-related ligand-receptor interactions in the early inflammatory phase (Figure S3d), which is consistent with previous studies suggesting inflammatory fibroblasts mediate macrophages through CCL2 and CCL7 chemokines [15].

To validate NLRP3's impact on macrophage recruitment, flow cytometry was performed on Day 2 wounds from WT and Nlrp3 KO mice. NLRP3 deficiency significantly reduced the proportion of total macrophages (F4/80+) and M1 macrophages (F4/80+, CD86+) in KO wounds (Figure 4e). Concordantly, qPCR analysis revealed marked downregulation of key chemotactic genes (e.g. *Ccl2/3/7*) in KO wounds (Figure 4d). To dissect the interplay between NLRP3 activation in macrophages and fibroblast migration, we employed a transwell co-culture system (Figure 4f). Firstly, LPS + ATP robustly activated the NLRP3 inflammasome in macrophages, as confirmed by Western blotting, while the NLRP3 inhibitor MCC950 suppressed its activation (Figure S4a). Secondly, LPS significantly upregulated *Ccl3* and *Ccl7* expression in macrophages, and LPS + ATP further increased their expression, while the NLRP3 inhibitor MCC950 suppressed inflammasome-activated chemokine expression (Figure 4g). Finally, as expected, LPS + ATP-primed macrophages significantly enhanced fibroblast migration, an effect abolished by MCC950 (Figure 4h), establishing NLRP3 as an enhanced mediator of macrophage-driven chemotaxis. Direct LPS + ATP stimulation further revealed NLRP3's cell-intrinsic role in fibroblasts: WT fibroblasts exhibited augmented migration, whereas Nlrp3 KO fibroblasts showed blunted responses (Figure S4b). These findings collectively indicate that NLRP3 inflammasome activation in both macrophages and fibroblasts enhances their chemotactic recruitment during the early inflammatory phase.

NOD-, LRR- and pyrin domain-containing protein 3 is involved in macrophage phenotype switching during wound healing

MAC-mediated immune regulation and inflammatory responses are critical for wound healing [24]. In the inflammatory phase of wound healing, Nlrp3−/− mice exhibited not only attenuated inflammatory responses (Figure 4b and c) but also a reduced proportion of pro-inflammatory M1 macrophages (Figure 4e). To clarify NLRP3's role in regulating macrophage pro- and anti-inflammatory phenotypes, we detected inflammation-related gene expression in WT and KO mouse wounds on days 2 and 7 post-injury. Results showed that in KO mouse wounds during the inflammatory phase, pro-inflammatory genes (*Il6*, *Il1β*, and *Nos2*) were downregulated, while anti-inflammatory genes (*Il10*, *Mrc1*, and *Tgfβ1*) were upregulated (Figure 5a). Similarly, even during the wound repair phase, the expression of pro-inflammatory genes (*Il1β*, *Tnfα*, and *Nos2*) was reduced in KO mouse wounds, while the expression of anti-inflammatory genes (*Arg1*, *Il10*, *Mrc1*, and *Tgfβ1*) was increased (Figure 5b).

Previous studies have shown that NLRP3 inflammasome activation promotes M1 macrophage polarization [24–26]. To explore this further, we induced M1 polarization in BMDMs with LPS, M2 polarization with IL-4, and NLRP3 inflammasome activation with LPS + ATP. PCR results revealed that LPS-induced M1 polarization mildly upregulated *Nlrp3* expression, IL-4-induced M2 polarization significantly downregulated *Nlrp3*, and LPS + ATP treatment markedly increased *Nlrp3* expression (Figure 5c). In addition, BMDMs from WT and *Nlrp3*-KO mice were induced by IL-4 *in vitro*. Flow cytometry analysis showed the proportion of M2 macrophages (F4/80+, CD11b+, CD206+) in NLRP3 KO BMDMs

Downloaded from academic.oup.com/burnstrauma/article/doi/10.1093/burnst/tkag002/8415534 by guest on 12 October 2026

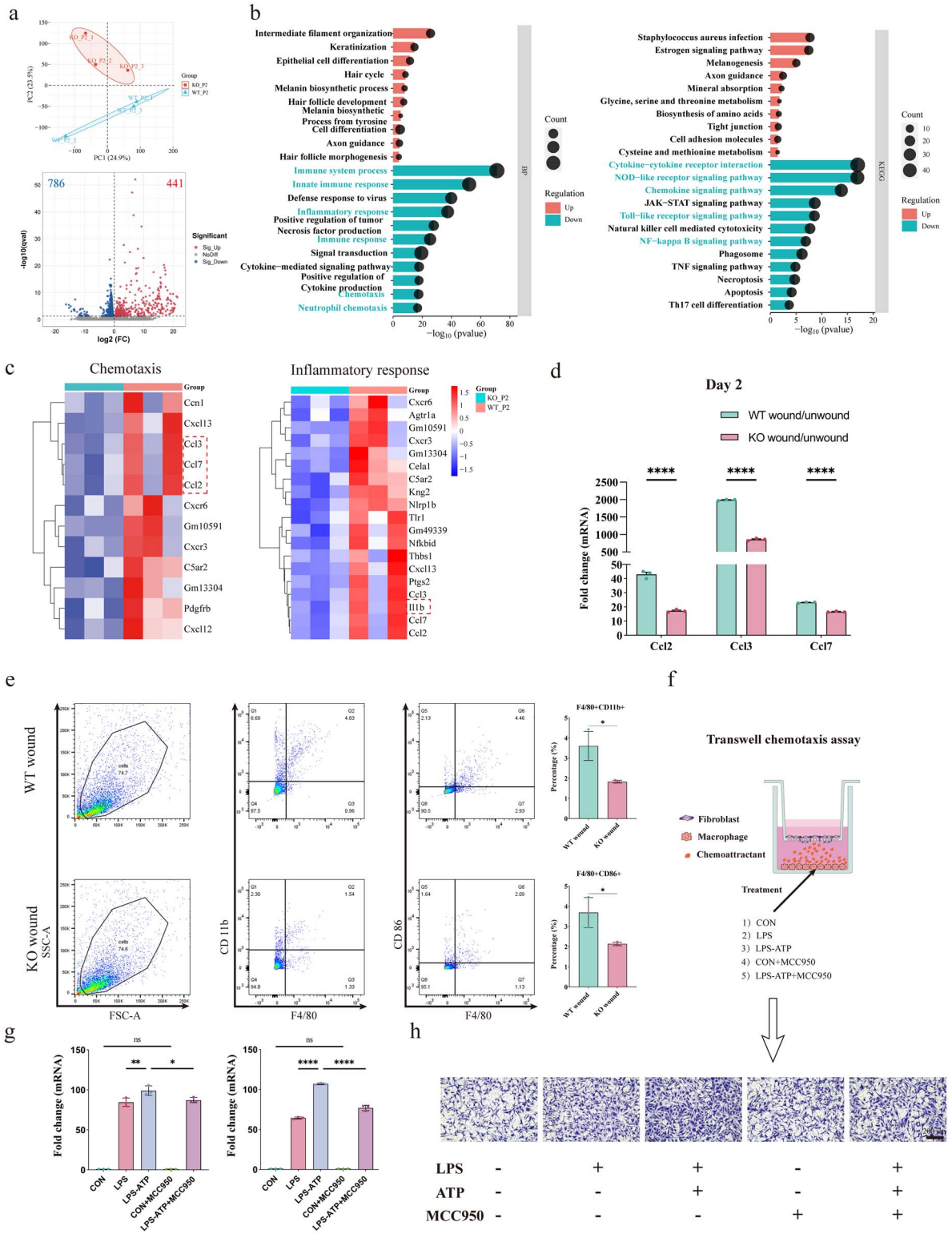


Figure 4 RNA sequencing combined with *in vivo* and *in vitro* experiments was used to verify the effects of NLRP3 KO on cell chemotaxis during the inflammatory phase. (**a**) Principal component analysis (PCA) and volcano plot of DEGs. Red dots represent significantly upregulated genes in KO compared to WT, while blue dots represent significantly downregulated genes (q-value <0.05, $|\log2 \text{ fold change}| > 1$). (**b**) GO and KEGG pathway enrichment analysis of DEGs between WT and KO mouse wounds. Left panel: GO enrichment analysis; right panel: KEGG pathway enrichment analysis; upregulated (red) and downregulated (blue) genes in KO mouse wounds. (**c**) Heatmap analysis of chemotaxis and inflammatory response-related genes in WT and KO mouse wounds at Day 2 post-injury. (**d**) qRT-PCR analysis of chemotaxis-related gene expression (*Ccl2*, *Ccl3*, and *Ccl7*) in WT and KO mouse wounds on Day 2 post-injury (mean ± SD, $n = 3$). (**e**) Flow cytometry analysis of macrophage proportion and M1 macrophage polarization in wound tissues on Day 2 post-injury (mean ± SD, $n = 3$). (**f**) Schematic representation of the Transwell chemotaxis assay for fibroblast migration in macrophage co-culture. (**g**) qRT-PCR analysis of chemotaxis-related gene expression (*Ccl3* and *Ccl7*) in macrophages through different treatments. (**h**) Representative crystal violet staining images in transwell assays to evaluate the effect of macrophage NLRP3 inflammasome activation on fibroblast migration. *PCA* principal component analysis, *DEG* differentially expressed gene, *GO* Gene ontology, *KO* NLRP3 knockout, *WT* wild-type

Downloaded from academic.oup.com/burnstrauma/article/doi/10.1093/burnst/tkag002/8415534 by guest on 12 October 2026

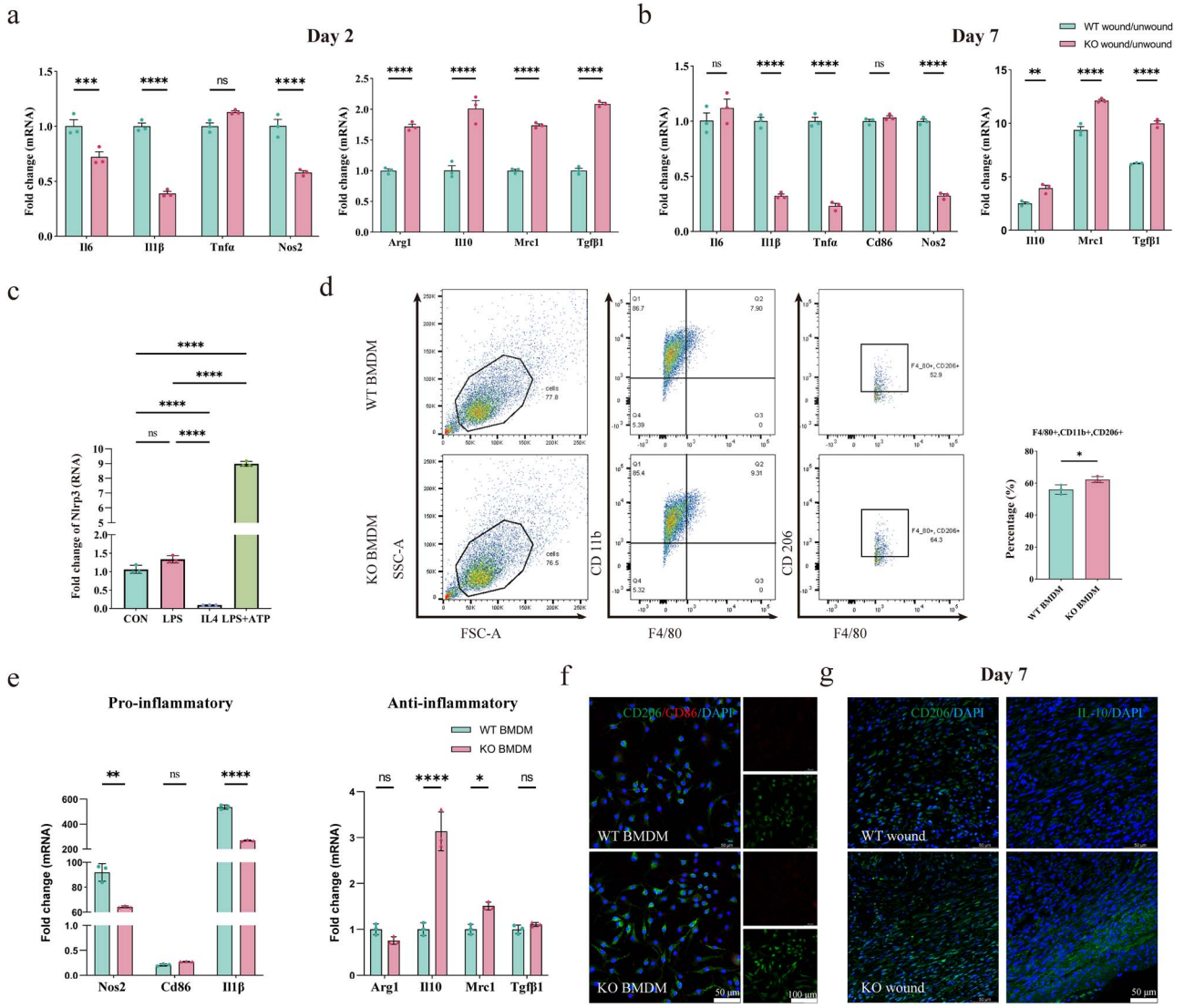


Figure 5 NLRP3 is involved in macrophage phenotype switching during wound healing. (**a**) qRT-PCR analysis of inflammation-related gene expression in WT and KO mouse wounds on Day 2 post-injury. (**b**) qRT-PCR analysis of inflammation-related gene expression in WT and KO mouse wounds on Day 7 post-injury. (**c**) qRT-PCR analysis of Nlrp3 expression in WT BMDM by different treatments. LPS: 1 μg/ml, 24 h; IL-4: 20 ng/ml, 48 h. LPS + ATP: LPS 250 ng/ml for 5 h, then the ATP 2 mM for 1 h. (**d**) Flow cytometry analysis of IL-4-induced M2 macrophage polarization in WT and KO BMDM. IL-4: 20 ng/ml, 48 h. (**e**) qRT-PCR analysis of pro-inflammatory and anti-inflammatory gene expression in WT and KO BMDMs (mean ± SD, $n = 3$). (**f**) Representative IF images of CD206 and CD86 expression in WT and KO BMDM induced by IL-4 (20 ng/ml, 48 h). CD206 (green), CD86 (red), and DAPI (blue). Scale bar, 50um. (**g**) Representative IF images of M2 polarization-related gene expression in WT and KO wounds at Day 7 post-injury. CD206 (green), IL-10 (green), and DAPI (blue). Scale bar, 50 μm. *LPS* lipopolysaccharide, *ATP* Adenosine Triphosphate, *IL* Interleukin, *BMDM* bone marrow-derived macrophage, *KO* NLRP3 knockout, *WT* wild-type

was increased (Figure 5d). qPCR analysis revealed that pro-inflammatory genes (*Nos2*, *IL-1β*) were downregulated, and anti-inflammatory genes (*Il10, Mrc1*) were significantly upregulated in Nlrp3 KO BMDMs compared to WT (Figure 5e). IF staining also confirmed increased expression of CD206 in KO BMDM (Figure 5f). These results indicate that, consistent with *in vivo* findings, Nlrp3 KO BMDMs are more prone to M2 polarization. In addition, IF images demonstrated that anti-inflammatory markers (CD206, IL-10) were upregulated in Nlrp3 KO wounds at 7 days post-injury. In summary, NLRP3 KO mice display a relatively lower inflammatory microenvironment, promoting macrophage polarization to the anti-inflammatory M2 type.

Single-cell sequencing data revealed NOD-, LRR- and pyrin domain-containing protein 3's regulatory role in the phenotypic switching of macrophages and fibroblasts during wound healing

Macrophages and fibroblasts, highly plastic cells, play a key role in wound healing [27–29]. To further explore the relationship between NLRP3 and the phenotypes of macrophages and fibroblasts during wound healing, we analyzed scRNA data of mouse

Downloaded from academic.oup.com/burnstrauma/article/doi/10.1093/burnst/tkag002/8415534 by guest on 12 October 2026

acute wounds via cell sub-clustering and functional annotation. The results showed that myeloid cells were subclustered into distinct subsets: M1 (pro-inflammatory), M2 (reparative), chemotaxis macrophage, and DC populations (DC1–2) based on functional gene signatures (Figure 6a and b). *Nlrp3* and *Il1b* expression was enriched in M1 and chemotaxis macrophage (Figure 6c). Functional annotation revealed that M1 macrophage upregulated innate immune pathways (e.g. NOD-like/TNF/NF-κB signaling), while chemotaxis macrophage preferentially activated leukocyte migration and chemotaxis (Figure 6d and e). This distinct functional partitioning indicates that NLRP3 inflammasome activation drives both M1 polarization and chemotactic recruitment.

Parallel sub-clustering of fibroblasts identified inflammatory fibroblasts, reparative fibroblasts, angiogenic fibroblasts, etc. (Figure 6f). *Nlrp3* and *Il1b* localized predominantly to inflammatory fibroblasts (Figure 6g). GO analysis highlighted leukocyte migration and immune cell activation as top-enriched pathways in *Nlrp3*-high inflammatory fibroblasts (Figure 6h and i). Strikingly, *Nlrp3*+ fibroblasts exhibited dual regulation: upregulation of chemotaxis/taxis pathways coincided with suppression of ECM remodeling genes (Figure 6j). The results further provide evidence that NLRP3's close link to cell chemotaxis and its regulatory role in macrophage and fibroblast phenotypes.

NOD-, LRR- and pyrin domain-containing protein 3 inflammasome affects fibroblast pro-repair phenotypic transition

Building on scRNA-seq evidence of suppressed ECM-related pathways in NLRP3+ fibroblasts (Figure 6j), we hypothesized that NLRP3 modulates fibroblast reparative transitions via IL-1 signaling. CellChat analysis identified neutrophils/macrophages as IL-1β sources during inflammation (Days 2–4), with fibroblasts/myo fibroblasts serving as key receivers (Figure 7a). Strikingly, the Il1b-(Il1r1 + Il1rap) axis dominated macrophage/fibroblast crosstalk, peaking in myo fibroblasts during inflammation (Figure 7b), suggesting macrophage-derived IL-1β directs fibroblast phenotypic transition. To investigate the association between fibroblast phenotype transitions and NLRP3 inflammasome activation, Subclustering analysis revealed nine dynamic fibroblast subsets with the main cluster 0–4 for the following analysis (Figure S6a and b). Clusters 0, 2, and 4 specialized in ECM remodeling, cluster 1 exhibited mixed inflammatory-reparative features, and cluster 3 emerged as a pro-inflammatory population enriched in cytokine signaling (Figure S6c and Table S3). Pseudotime trajectory modeling positioned cluster 0 as the progenitor state, progressively diverging into terminal inflammatory (cluster 3) and reparative phenotypes (cluster 2) (Figure 7c). Reparative fibroblasts exhibited higher differentiation states than inflammatory fibroblasts, suggesting a potential transition from inflammatory to reparative phenotypes during wound healing, which is in line with Yuval Rinkevich's study that pro-inflammatory fibroblasts can serve as an intermediate state before switching to repair-associated myo fibroblasts [30]. Further analysis of *Nlrp3* and *Il1b* revealed their predominant expression in state 1 (inflammatory fibroblasts) and state 5 (reparative fibroblasts), linking NLRP3 inflammasome activation to both inflammatory and reparative fibroblast phenotypes (Figure 7d). Screening for key genes regulating this differentiation trajectory identified IL-1β, Spp1, Lgals7, Saa3, and Cxcl2 as significantly upregulated in later clusters, suggesting roles in inflammation, chemotaxis, and tissue remodeling (Figure 7e). Thus, NLRP3 inflammasome activation influences fibroblast phenotypes, impacting both their pro-inflammatory and reparative functions.

Functional validation in Nlrp3−/− mice demonstrated that under homeostatic conditions (without injury or stimulation), Nlrp3−/− mice show downregulation of Acta2, Col1a1, Col3a1, Cd31, Vegfa, etc (Figure 7f). Similarly, *in vitro*-isolated primary dermal fibroblast cells from *Nlrp3*−/− mice exhibit downregulation of repair-related markers like Acta2 and Col1a1 (Figure 7g and h). Unexpectedly, Nlrp3 deficiency fibroblasts concomitantly enhanced proliferation and migration (Figure S5d and e). Fibroblasts could transform into myo fibroblasts to promote ECM synthesis and wound contraction during wound repair. To mimic inflammasome activation, we treated WT and KO fibroblasts with LPS + ATP *in vitro* and performed collagen contraction assays. Both groups showed reduced contractile ability after inflammatory stimulation (Figure S5f).

To investigate macrophage-mediated effects on fibroblast function, we established an macrophage-fibroblast co-culture model mimicking an *in vivo* inflammatory microenvironment (Figure 7i). Stimulation with LPS + ATP induced *Nlrp3* expression in fibroblasts, which was further enhanced when co-cultured with NLRP3-activated macrophages (Figure 7j). Analysis of macrophage NLRP3 inflammasome activation revealed its inhibitory effects on fibroblast reparative genes and proteins (α-SMA, COL1, and TGFβ1), which were attenuated in Nlrp3 KO fibroblasts (Figure 7k, l and l). Interestingly, while macrophage NLRP3 inflammasome activation suppressed fibroblast reparative function, it promoted fibroblast proliferation and migration (Figure S5g and h). Collectively, these findings indicate that NLRP3 inflammasome activation regulates the fibroblasts' functions and phenotypy through both intrinsic and macrophage-mediated mechanisms.

NOD-, LRR- and pyrin domain-containing protein 3 induces reactive oxygen species and modulates Smad-dependent fibroblast activation independent from inflammasome

Inflammasome activation in macrophages inhibits the pro-reparative phenotype of fibroblasts in a manner linked to fibroblast-intrinsic NLRP3 expression. We hypothesized that this effect is mediated by IL-1β, the principal effector cytokine released upon inflammasome activation. Consistent with this premise, exogenous IL-1β markedly up-regulated NLRP3 transcription while simultaneously suppressing the pro-reparative gene signature of fibroblasts (Acta2 and Col1a1; Figure S6b). Unexpectedly, exposure of fibroblasts to the canonical inflammasome trigger LPS plus ATP failed to generate detectable cleaved caspase-1 (p20), in contrast to the activation observed in macrophages (Figures 8a and b, and S6a). In light of previous reports on NLRP3-mediated regulation of non-immune cells [31–33], we postulated that

Downloaded from academic.oup.com/burnstrauma/article/doi/10.1093/burnst/tkag002/8415534 by guest on 12 October 2026

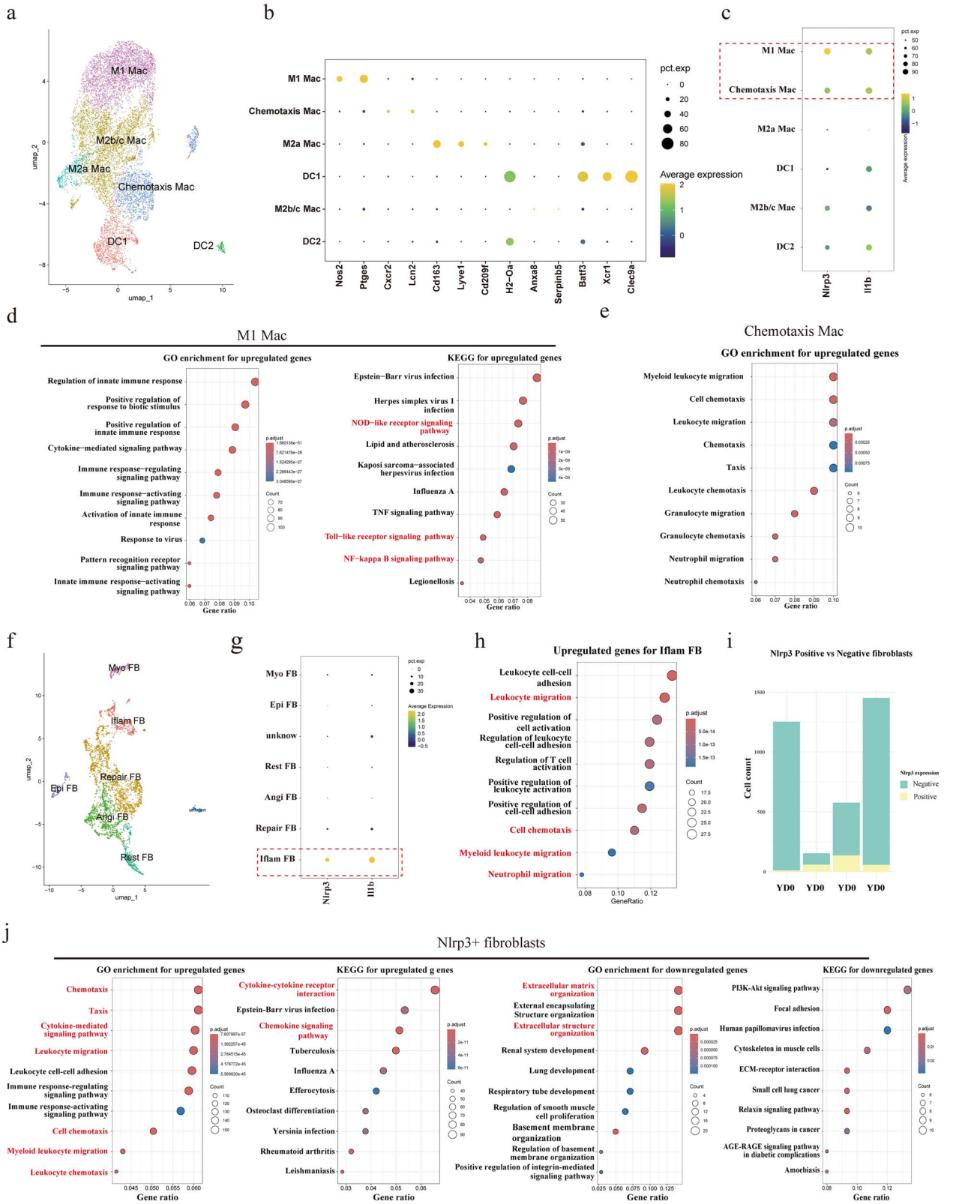


Figure 6 Single-cell sequencing data reveal NLRP3's regulatory role in the phenotypic switching of macrophages and fibroblasts during wound healing. (**a**) UMAP visualization of myeloid cells showing subpopulations. (**b**) Dotplot showing marker genes for myeloid cell subsets. (**c**) Dot plot illustrating the expression levels of key inflammasome activation genes (*Nlrp3*, *Il1b*) in different myeloid cell subpopulations. (**d**) GO and KEGG enrichment analysis of highly variable genes upregulated in M1 macrophages. (**e**) GO enrichment analysis of highly variable genes upregulated in chemotaxis macrophage. (**f**) UMAP visualization of fibroblasts showing fibroblast subpopulations epi fibroblast: epidermal fibroblast, angi fibroblast: angiogenic, inflam fibroblast: inflammatory fibroblast, and repair fibroblast: reparative fibroblast. (**g**) Dot plot illustrating the expression levels of key inflammasome activation genes (*Nlrp3* and Il1b) in different fibroblast cell subpopulations. (**h**) GO enrichment analysis of highly variable genes upregulated in inflammatory fibroblasts (inflam fibroblast). (**i**) Temporal dynamics of NLRP3-positive fibroblast cells during wound healing. (**j**) GO and KEGG enrichment analysis of up-regulated and down-regulated genes in NLRP3-positive fibroblast compared with NLRP3-negative fibroblast. *LPS* lipopolysaccharide, *ATP* Adenosine Triphosphate, *IL* interleukin, *KO* NLRP3 knockout, *WT* wild-type

Downloaded from academic.oup.com/burnstrauma/article/doi/10.1093/burnst/tkag002/8415534 by guest on 12 October 2026

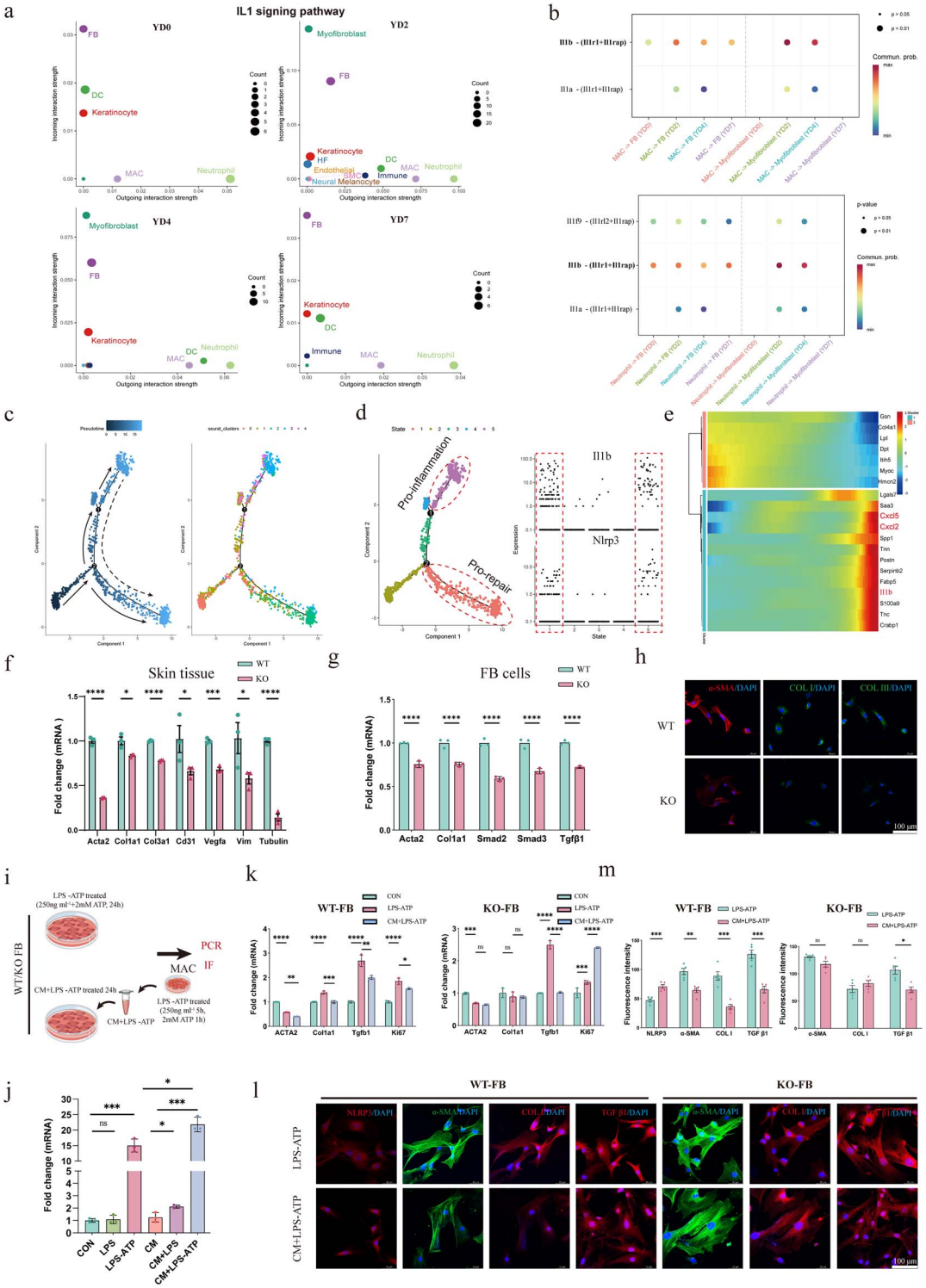


Figure 7 NLRP3 inflammasome affects fibroblast pro-repair phenotypic transition. (**a**) CellChat analysis of IL1 signaling pathway interaction strengths among cell populations at different time points during wound healing. (**b**) Interactions between macrophages, neutrophils, and fibroblasts via IL signaling pathways during wound healing. (**c**) Pseudotime analysis of fibroblast differentiation trajectories. (**d**) Expression of inflammasome-related genes (*Nlrp3* and Il1b) in fibroblast across different differentiation states. (**e**) The heatmap of the top 20 key genes driving fibroblast differentiation during wound healing. (**f**) qRT-PCR analysis of wound healing-related gene expression in skin tissue (unwound) from WT and KO mice (mean ± SD, $n = 3$). (**g**) qRT-PCR analysis of wound healing-related gene expression in primary fibroblast from WT and KO mice (mean ± SD, $n = 3$). (**h**) Representative IF images of wound healing-related protein expression in fibroblast from WT and KO mice. A-SMA (red), COLI and COLIII (green), DAPI (blue). Scale bar, 100 μm. (**i**) Schematic representation of the co-culture experiment using macrophage-CM and fibroblasts. Fibroblasts were derived from WT or NLRP3 KO mice. LPS -ATP-treated fibroblasts: fibroblasts were treated with LPS (250 ng/ml) and ATP (2 mM) for 24 h. CM + LPS-ATP treated fibroblasts: CM collected from LPS-ATP treated macrophages (250 ng/ml LPS for 5 h, 2 mM ATP for 1 h) was applied to fibroblasts for 24 h. (**j**) qRT-PCR analysis of NLRP3 mRNA expression in fibroblasts under different treatment conditions. (**k**) qRT-PCR analysis of wound healing-related gene expression in WT and KO fibroblasts after treatment with LPS + ATP or CM + LPS + ATP (mean ± SD, $n = 3$). (**l**) Representative IF images of wound healing-related protein expression in WT and KO fibroblasts after treatment with LPS + ATP or CM + LPS + ATP. Scale bar, 100 μm. (**m**) Quantitative analysis of IF images for wound healing-related protein expression in WT and KO fibroblasts from (l) (mean ± SD, $n = 3$). *LPS* lipopolysaccharide, *ATP* Adenosine Triphosphate, *IL* interleukin, *KO* NLRP3 knockout, *WT* wild-type

Downloaded from academic.oup.com/burnstrauma/article/doi/10.1093/burnst/tkag002/8415534 by guest on 12 October 2026

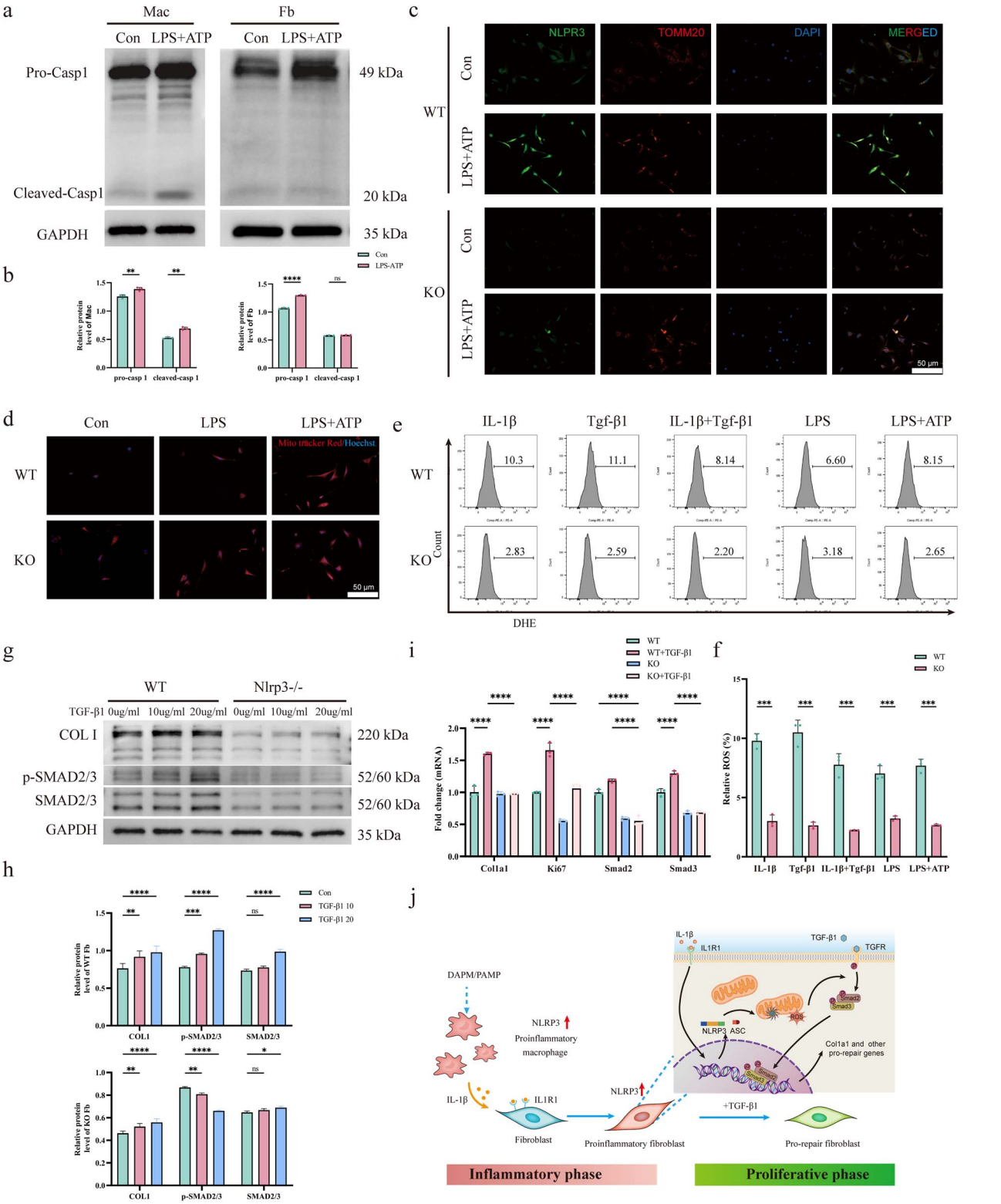


Figure 8 NLRP3 protein induces ROS and modulates Smad-dependent fibroblast activation independent from inflammasome. (**a**) Western blot analysis of pro-casp1 and cleaved casp1 protein expression in macrophage and fibroblast under different treatments. GAPDH was used as a loading control. LPS (500 ng/ml, 4.5 h) plus ATP (5 mM, 1 h). (**b**) Quantification of pro-casp1 and cleaved casp1 protein levels, normalized to GAPDH (mean ± SD, $n = 3$). (**c**) Representative IF images of NLRP3 (green), TOMM20 (red) and DAPI (blue) in WT and KO fibroblast with different treatments. Scale bar, 50 μm. (**d**) Representative IF images of MitoTracker (red) of WT and KO fibroblast with different treatments. Cell nuclei are counterstained with Hoechst (blue). Scale bar, 50 μm. (**e**) Flow cytometry analysis of ROS level of WT and KO fibroblast with different treatments by Dihydroethidium (DHE) staining. (**f**) Quantification of ROS level of WT and KO fibroblast with different treatments (mean ± SD, $n = 3$). (**g**) Western blot analysis of COL1, p-SMAD 2/3, and SMAD2/3 protein expression of WT and KO fibroblast with different concentrations of TGFβ1. GAPDH was used as a loading control. (**h**) Quantification of Col1, p-SMAD 2/3, and SMAD2/3 protein levels of WT and KO fibroblast with different concentrations of TGFβ1 (mean ± SD, $n = 3$). (**i**) qRT-PCR analysis of *Col1a1*, *Ki67*, *Smad2*, and *Smad3* in fibroblast through different treatments (mean ± SD, $n = 3$). (**j**) Schematic representation of the molecular mechanisms by which NLRP3 regulates fibroblast function. *ATP* Adenosine Triphosphate, *ROS* reactive oxygen species, *DHE* Dihydroethidium, *KO* NLRP3 knockout, *WT* wild-type

Downloaded from academic.oup.com/burnstrauma/article/doi/10.1093/burnst/tkag002/8415534 by guest on 12 October 2026

NLRP3 governs fibroblast behavior independently of canonical inflammasome assembly.

Immunofluorescence staining revealed a pronounced co-localization of endogenous NLRP3 with the mitochondrial marker TOMM20 in WT fibroblasts (Pearson's R = 0.66; Figures 8c and S6c). Over-expression of NLRP3 further increased this co-localization (R = 0.75; Figure S6c), suggesting a direct mitochondrial association. Functional interrogation using mitochondrial membrane-potential dyes demonstrated that NLRP3 activation enhanced mitochondrial activity, whereas NLRP3 deficiency attenuated the LPS/ATP-induced impairment of mitochondrial function (Figures 8d). Flow-cytometric quantification of ROS showed consistently lower levels in Nlrp3 KO fibroblasts under all experimental conditions relative to WT controls (Figures 8e and f), despite comparable up-regulation of NLRP3 expression by the various stimuli (S6a, b, and d).

TGF-β1 is the dominant driver of fibroblast-mediated repair, and the Smad pathway is a critical determinant of fibroblast functionality. Stimulation of WT fibroblasts with TGF-β1 induced Smad2/3 phosphorylation (p-Smad2/3) and elevated COL1 expression; these responses were markedly attenuated in Nlrp3 KO fibroblasts (Figure 8g–i). In addition, treatment with LPS + ATP up-regulates the fibroblast NLRP3 inflammasome; subsequent exposure to TGF-β1 further enhanced the activation of Smad signaling (Figure S6d). Integrating these findings with previous evidence that NLRP3 promotes renal and cardiac fibrosis via inflammasome-independent mechanisms [34, 35], we propose that macrophage inflammasome activation drives IL-1β secretion which engages IL-1R1 on fibroblasts, triggering NF-κB-dependent NLRP3 up-regulation that fosters a pro-inflammatory and anti-reparative phenotype during inflammation. NLRP3, in turn, co-localizes with mitochondria to amplify ROS production, thereby potentiating TGF-β1-induced Smad phosphorylation and subsequent expression of repair-associated genes and proteins, including COL1 (Figure 8j).

NOD-, LRR- and pyrin domain-containing protein 3 knockout promotes hair follicle and nerve repair during the wound repair phase

Histological assessments at Day 14 post-injury demonstrated reduced scarring and augmented hair follicle morphogenesis in Nlrp3 KO versus WT wounds (Figure 2). Transcriptomic profiling of Day 7 repair-phase tissues revealed NLRP3 deficiency broadly downregulated inflammatory/immune pathways while upregulating regenerative programs encompassing collagen remodeling, hair follicle induction, and neural regeneration (Figure 9a–c). Specifically, to delineate the temporal dynamics driving differential healing outcomes, we performed Mfuzz time-series clustering on transcriptomic data spanning the wound repair (Days 0–14). Genes stratified into 10 distinct co-expression clusters, with functional annotation revealing divergent activation trajectories between genotypes across three pivotal modules. In WT wounds, inflammatory and immune-regulatory clusters exhibited rapid upregulation, peaking at Day 2 post-injury. In contrast, Nlrp3 KO wounds displayed a delay in inflammatory activation, with cluster 6 reaching maximal expression intensity 2 days later than WT. Conversely, hair follicle, neural regeneration, and Wnt signaling clusters in KO wounds achieved rapidly elevated expression by Day 7 and sustained high levels through Day 14, diverging from the delayed activation observed in WT controls (Figure 9d). As noted earlier, RNA sequencing results indicated upregulation of pathways related to hair follicle and nerve regeneration in Nlrp3 KO mice. IF staining on Day 14 confirmed increased hair follicle density and enhanced nerve regeneration in Nlrp3 KO wounds compared to WT (Figure 9e). This supports the hypothesis that NLRP3 deficiency facilitates hair follicle and nerve repair.

In vivo neutralization of interleukin-1 beta attenuates inflammatory cell infiltration and macrophage pro-inflammatory polarization while impairing wound closure

To clarify the contribution of IL-1β—the principal effector downstream of the NLRP3 inflammasome—to cutaneous wound healing, we administered a neutralizing anti-IL-1β antibody subcutaneously on post-wound days 0, 1, 3, and 5, coincident with the increased endogenous expression of IL-1β (Figure 10a). ELISA and western blot analyses of wound on days 2 and 4 confirmed that the antibody markedly reduced local IL-1β abundance (Figures 10b and S7a and b).

In vivo neutralization of IL-1β significantly delayed wound closure (Figures 10c–e and S8a) and suppressed the expression of COL1, α-SMA, and TGF-β1 on Day 7 (Figure S8b and c). IF analyses specifically evaluating macrophage and neutrophil dynamics revealed that IL-1β blockade markedly inhibited the pro-inflammatory macrophage phenotype ($F4/80^+CD86^+$) while promoting a pro-reparative phenotype ($F4/80^+CD206^+$) during both the inflammatory (days 2 and 4) and proliferative (Day 7) phases. Additionally, neutrophil ($Ly6G^+$) infiltration on Day 2 was significantly reduced (Figure 10h–k and Figure S7c and d). These data indicate that IL-1β is a pivotal inflammatory mediator in wound repair; its depletion not only attenuated inflammatory-cell infiltration during the early inflammatory phase (Day 2) but also impaired the subsequent recruitment of cells on Day 4 (Figure 10f and g). Masson trichrome and IF staining of wounds at the remodeling phase (Day 14) demonstrated that neutralization of IL-1β augmented collagen deposition and elevated COL1 and α-SMA expression, thereby intensifying post-healing fibrosis (Figure S7a and d). Collectively, these findings establish IL-1β as the principal NLRP3-derived effector, is indispensable for physiological wound healing. Reducing its availability not only retards the healing process but also predisposes to exaggerated scar formation.

Interleukin-1 beta replenishment in NOD-, LRR- and pyrin domain-containing protein 3-deficient mice restores inflammatory cell infiltration and pro-inflammatory macrophage polarization to accelerate wound closure

Prior studies indicated that the impaired wound healing observed in NLRP3-deficient mice results primarily from attenuated

Downloaded from academic.oup.com/burnstrauma/article/doi/10.1093/burnst/tkag002/8415534 by guest on 12 October 2026

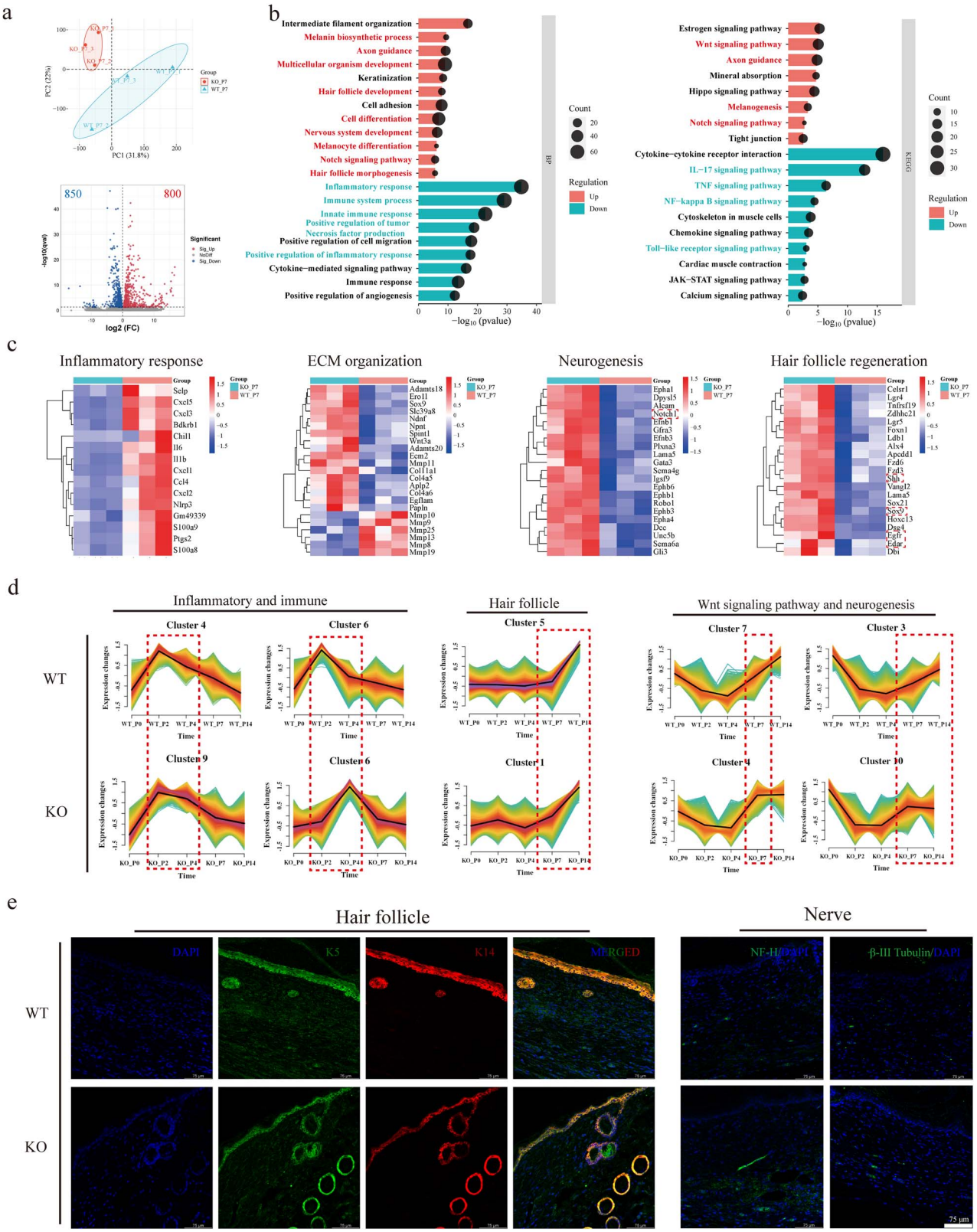


Figure 9 NLRP3 KO promotes hair follicle and nerve repair during the wound repair phase. (**a**) PCA and volcano plot of DEGs. Red dots represent significantly upregulated genes in KO compared to WT, while blue dots represent significantly downregulated genes (p-value <0.05, |log2 fold change| > 1). (**b**) GO and KEGG pathway enrichment analysis of DEGs between WT and KO mouse wounds. Left panel: GO enrichment analysis; right panel: KEGG pathway enrichment analysis; upregulated (red) and downregulated (blue) genes in KO mouse wounds. (**c**) Heatmap analysis of inflammatory response-related, ECM organization, neurogenesis, and hair follicle regeneration-related genes in WT and KO mouse wounds at Day 7 post-injury. (**d**) Mfuzz analysis showing dynamic changes of inflammation, immune response, hair follicle regeneration, Wnt Signaling pathway, and neuroregeneration-related genes in WT and KO mouse wounds. The red dashed box highlights the time points with the most significant differences between the two groups. (**e**) Representative IF images of hair follicle and nerve markers expression in WT and KO wounds at Day 14 post-injury. K5 (green), K14 (red), NF-H (green), and β-III tubulin (green), and DAPI (blue). Scale bar, 75 μm. *PCA* principal component analysis, *DEG* differentially expressed genes, *KO* NLRP3 knockout, *WT* wild-type

Downloaded from academic.oup.com/burnstrauma/article/doi/10.1093/burnst/tkag002/8415534 by guest on 12 October 2026

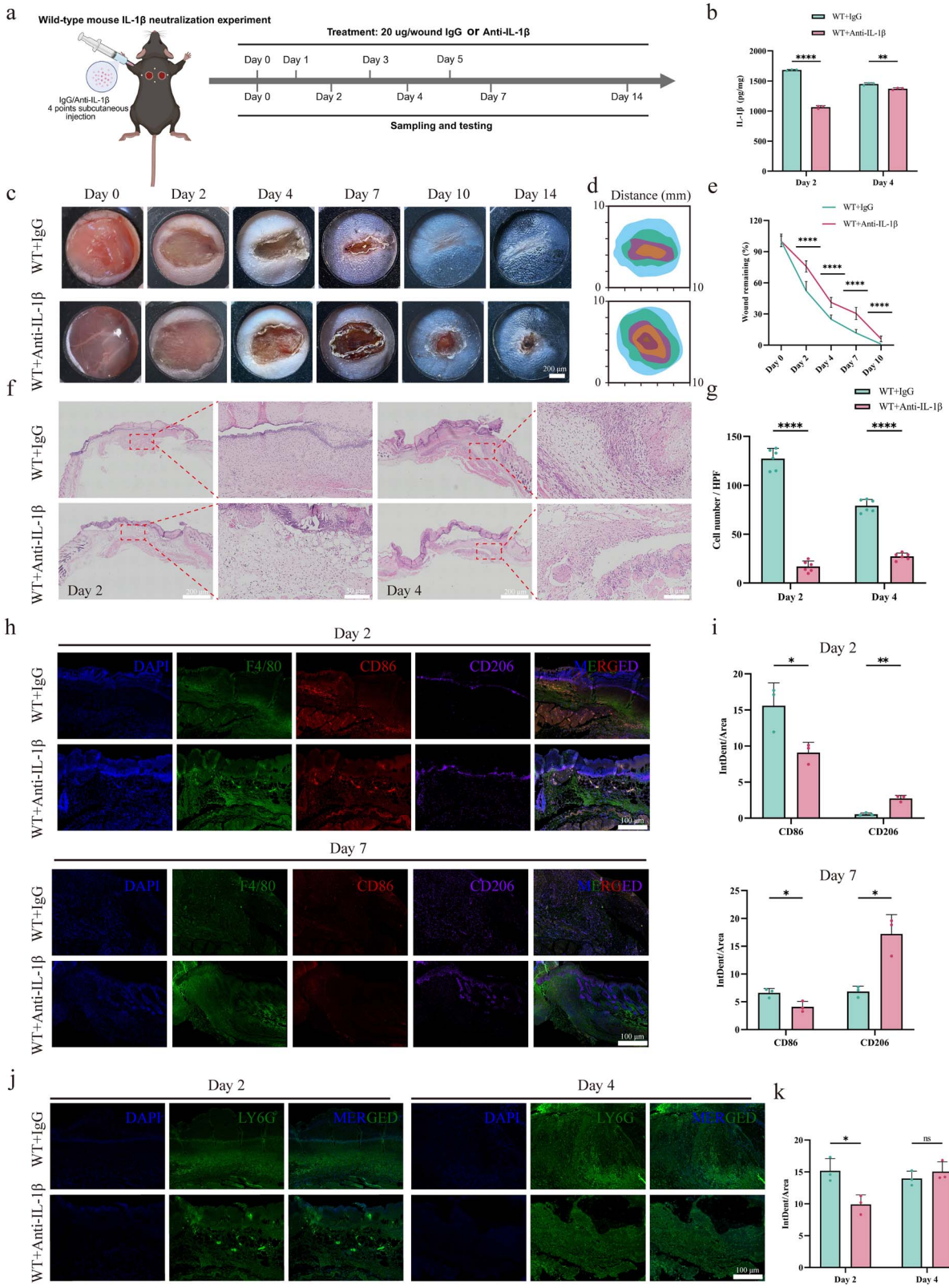


Figure 10 Effects of *in vivo* IL-1β blockade on wound healing and inflammatory infiltration. (**a**) Schematic representation of the different treatments of the WT mouse. (**b**) ELISA analysis of the IL-1β level of wound tissue on the different treatments. (**c**) Representative optical images of wounds on days 0, 2, 4, 7, and 14. Scale bar, 200 μm. (**d**) Wound area tracing analysis corresponding to (c). (**e**) Quantitative analysis of relative wound area on days 2, 4, 7, and 10 from (c).(mean $\pm$ SD, $n = 6$). (**f**) Representative H&E staining of wounds on days 2 and 4. Scale bar, 200 and 50 μm. (**g**) The quantification analysis of cell number per HPF in the wound from (f). (mean $\pm$ SD, $n = 6$). (**h**) Representative IF images of F4/80 (green), CD86 (red), and CD206 (purple) for Day 2 and Day 7. Cell nuclei are counterstained with DAPI (blue). Scale bar, 100 μm. (**i**) Quantitative analysis of the IF area of CD86 and CD206 in the wound from (h). (mean $\pm$ SD, $n = 6$). (**j**) Representative IF images of LY6G (green) for Day 2 and Day 4. Cell nuclei are counterstained with DAPI (blue). Scale bar, 100 μm. (**k**) Quantitative analysis of the IF area of LY6G in the wound from (j).(mean $\pm$ SD, $n = 6$). *KO* NLRP3 knockout

Downloaded from academic.oup.com/burnstrauma/article/doi/10.1093/burnst/tkag002/8415534 by guest on 12 October 2026

IL-1β signaling. To verify this causality, we restored the physiological IL-1β landscape in Nlrp3−/− animals by subcutaneous administration of recombinant IL-1β (2 μg on Day 0, 10 μg on Days 1 and 3, and 2 μg on Day 5) to recapitulate the endogenous temporal gradient (Figure 11a). ELISA and western blot analyses of wound tissue collected on days 2 and 4 confirmed a pronounced and sustained rise in local IL-1β abundance (Figures 11b and S9a and b).

IL-1β reconstitution accelerated wound closure in Nlrp3−/− mice (Figures 11c–e and S10a) and increased the expression of COL1, α-SMA, and TGF-β1 on Day 7 (Figure S10b and c). In addition, IL-1β supplementation augmented early inflammatory-cell infiltration on Day 2, and increased the subsequent recruitment of reparative fibroblast populations on Day 4 (Figure 11f and g). IF analyses specifically evaluating macrophage and neutrophil dynamics revealed that IL-1β supplementation markedly promoted the pro-inflammatory macrophage phenotype ($F4/80^+CD86^+$) while suppressed a pro-reparative phenotype ($F4/80^+CD206^+$) on days 2, 4 and 7 (Figure 11h and i, and Figure S9c and d). Additionally, neutrophil ($Ly6G^+$) infiltration on Day 2 was significantly increased (Figure 11j and k). Masson trichrome and IF staining of wounds at the remodeling phase (Day 14) demonstrated that supplement of IL-1β augmented collagen deposition and elevated COL1 and α-SMA expression, thereby intensifying post-healing fibrosis (Figure S9a and d).

Spatiotemporal dynamic activation of the NOD-, LRR- and pyrin domain-containing protein 3 inflammasome during human wound healing

To characterize the spatiotemporal activation landscape of the NLRP3 inflammasome in acute human wound healing, we analyzed bulk RNA sequencing (GSE174661) and single-cell RNA sequencing (GSE241132) data from public databases. The results showed that NLRP3 gene expression was highest in the early inflammatory phase of wound healing (Wound1), then gradually decreased, but remained at a relatively high level during the repair phase (Wound7), ∼2–3 times the NLRP3 expression in normal skin. Additionally, NLRP3 expression was also at a high level in chronic wounds (venous ulcers) (Figure 12a). Further GSEA analysis was performed by pairwise comparison of normal skin, venous ulcers, and skin wounds on Day 1 and Day 7. The results indicated that the Nod-like receptor signaling pathway, which is highly associated with NLRP3 inflammasome activation, was significantly upregulated in the early inflammatory phase (Wound1) compared to normal skin and the repair phase (Wound7). Similarly, the Nod-like receptor signaling pathway was also significantly upregulated in venous ulcers compared to normal skin (Figure 12b and Figure S11a). These findings suggest that the NLRP3 inflammasome has a similar activation pattern in human and mouse acute skin wounds, and the sustained activation of the NLRP3 inflammasome may be related to the formation of chronic wounds.

Analysis of the single-cell sequencing data from human skin wounds revealed that the *NLRP3* and *IL-1β* gene were primarily expressed in macrophages and DCs, with extremely low expression in other cell types, such as epidermal cells and fibroblasts (Figure 12c and d, and Figure S11b and c). Further analysis of the expression of IL1 signaling pathway ligand-receptor pairs during wound healing showed that the expression pattern of IL-1β in macrophages was similar to the inflammasome activation pattern observed in bulk RNA sequencing. IL1R1, as the main ligand for IL-1β, was highly expressed not only in macrophages, DCs, and other myeloid cells but also in fibroblasts, endothelial cells, and vascular smooth muscle cells. The expression pattern of IL1R1 was consistent with the dynamic changes from the inflammatory phase to the repair phase of wound healing, suggesting that the activation of the NLRP3 inflammasome in myeloid cells, primarily macrophages, may promote the release of inflammatory factors such as IL-1β, thereby regulating the function of fibroblasts and endothelial cells during wound healing (Figure 12e).

Focusing on macrophage heterogeneity, subclustering identified a distinct NLRP3 high subset (Cluster 3) enriched for inflammasome components (NLRP3, IL-1B, CASP1), peaking during inflammation and declining dynamically post-repair (Figure 12f–h). KEGG pathway analysis of Cluster 3 highlighted upregulated immune cell migration and cytokine production pathways (Figure 12i), aligning with bulk RNA-seq chemokine trends. Furthermore, we analyzed the expression of ligands for the CCL and CXCL signaling pathways in human wounds. The results showed that CXCL12 was mainly expressed in fibroblasts, CCL3 was primarily expressed in macrophages, and CCL2 was highly expressed in vascular smooth muscle cells, endothelial cells, fibroblasts, and macrophages (Figure S11d). These findings suggest that the activation of NLRP3 in human skin wound healing may also be related to the chemotaxis of various cells to the wound site. To further support cross-species relevance, we performed a comparative bioinformatic analysis of NLRP3 gene and protein sequences from five mammalian species (mouse, rat, human, bovine, and rhesus macaque). This revealed >92% amino-acid identity in the NACHT and LRR domains which are critical for inflammasome assembly, indicating strong functional conservation (Figure S12). In conclusion, the activation of the NLRP3 inflammasome exhibits a similar spatiotemporal dynamic expression pattern and function in human and mouse wound healing processes, suggesting similar functions.

NOD-, LRR- and pyrin domain-containing protein 3 inflammasome orchestrates the migration of human-derived macrophages and fibroblasts

To determine whether NLRP3 inflammasome activation regulates the migration of human-derived macrophages and fibroblasts, we first stimulated THP-1 cells with LPS + ATP to trigger the NLRP3 inflammasome and applied the selective small-molecule inhibitor MCC950 to block its activation. Transwell assays revealed that inflammasome activation markedly enhanced THP-1 cell migration, while MCC950-mediated inhibition significantly attenuated it. Subsequent co-culture transwell experiments demonstrated that activation of the inflammasome in THP-1 cells robustly promoted HSF migration, whereas MCC950 treatment partially reversed this effect (Figure 13a). qPCR analyses of THP-1 cells demonstrated that inflammasome activation up-regulated

Downloaded from academic.oup.com/burnstrauma/article/doi/10.1093/burnst/tkag002/8415534 by guest on 12 October 2026

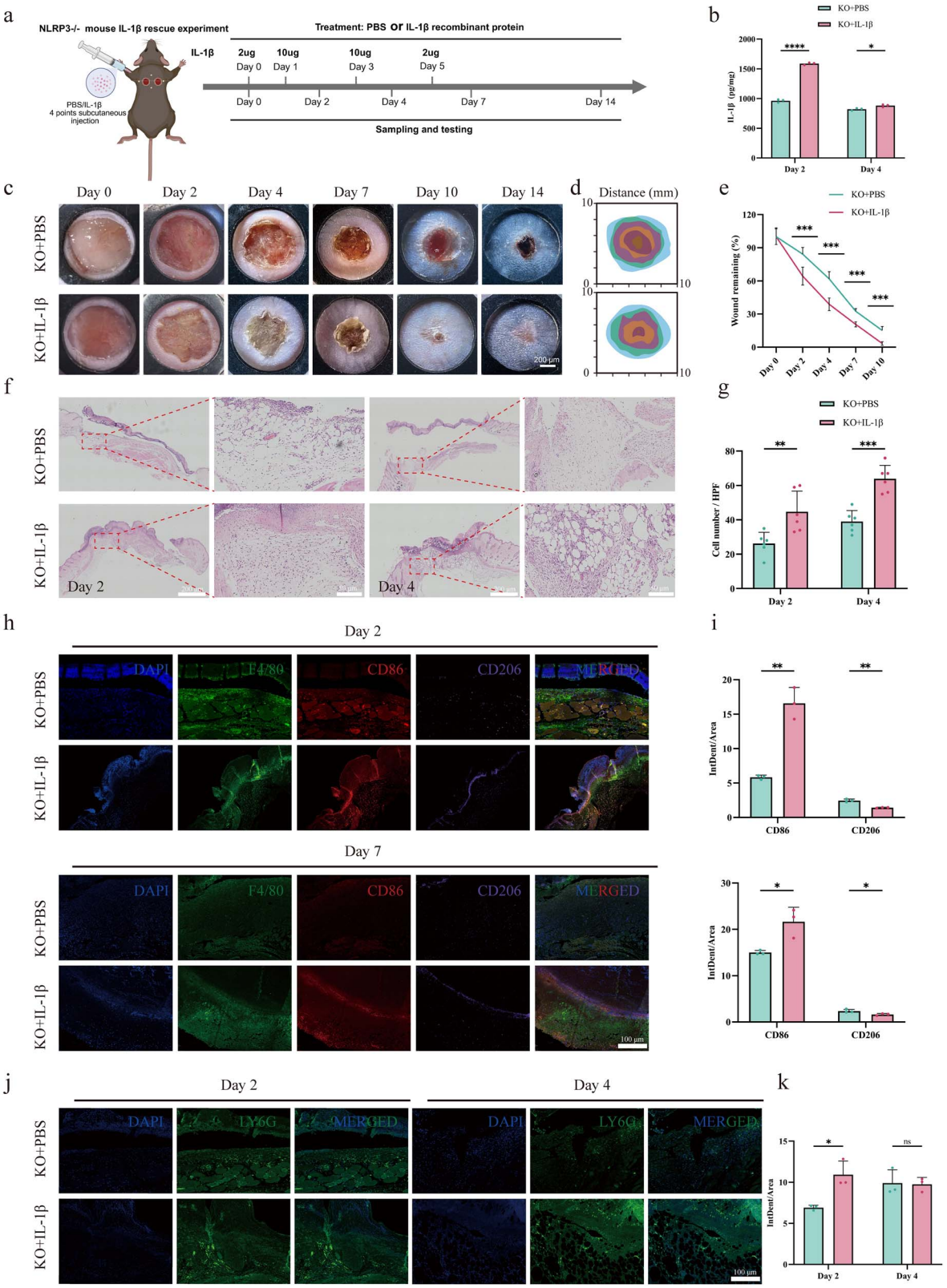


Figure 11 Impact of IL-1β replenishment on wound closure and inflammatory infiltration in NLRP3-deficient mice. (**a**) Schematic representation of the different treatments of the Nlrp3−/− mouse. (**b**) ELISA analysis of the IL-1β level of wound tissue on the different treatments (mean ± SD, $n = 6$). (**c**) Representative optical images of wounds and wound area tracing analysis corresponding to optical images on days 0, 2, 4, 7, and 14. Scale bar, 200 μm. (**d**) Wound area tracing analysis corresponding to optical images on Day 0, 3, 7, and from (c). (**e**) Quantitative analysis of relative wound area on days 2, 4, 7, and 10 from (c). (mean ± SD, $n = 6$). (**f**) Representative H&E staining of wounds on days 2 and 4. Scale bar, 200 and 50 μm. (**g**) The quantification analysis of cell number per HPF in the wound from (f). (mean ± SD, $n = 6$). (**h**) Representative IF images of F4/80 (green), CD86 (red), and CD206 (purple) for Day 2 and Day 7. Cell nuclei are counterstained with DAPI (blue). Scale bar, 100 μm. (**i**) Quantitative analysis of the IF area of CD86 and CD206 in the wound from (h). (mean ± SD, $n = 6$). (**j**) Representative IF images of LY6G (green) for Day 2 and Day 4. Cell nuclei are counterstained with DAPI (blue). Scale bar, 100 μm. (**k**) Quantitative analysis of the IF area of LY6G in the wound from (j). (mean ± SD, $n = 6$). *KO* NLRP3 KO, *WT* wild-type

Downloaded from academic.oup.com/burnstrauma/article/doi/10.1093/burnst/tkag002/8415534 by guest on 12 October 2026

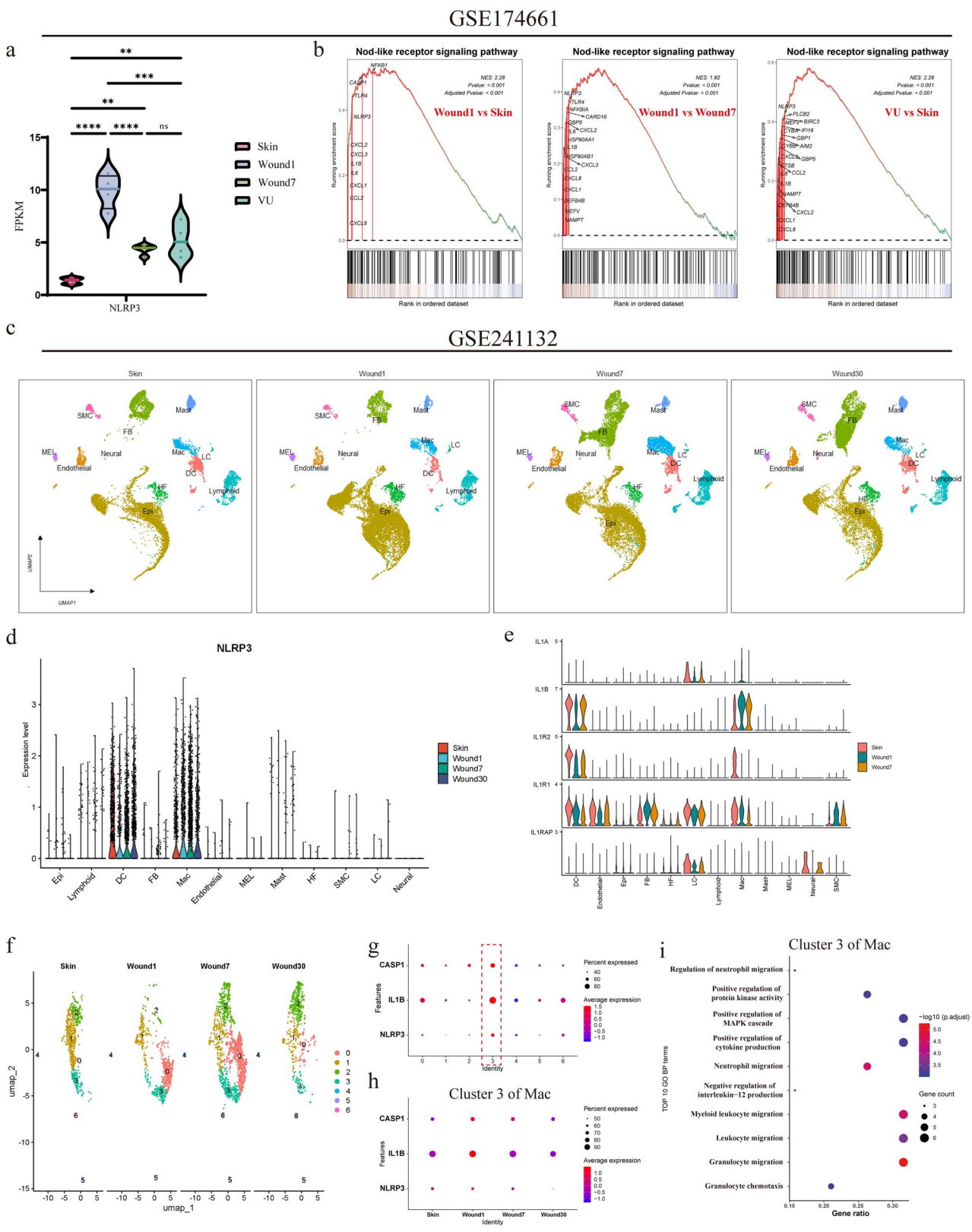


Figure 12 Spatiotemporal dynamics activation of the NLRP3 Inflammasome during human wound healing. (**a**) Transcriptomic analysis based on the GSE174661 dataset reveals dynamic expression of NLRP3 during wound healing. (**b**) GSEA analysis of the NOD-like receptor Signaling pathway between two groups. The top-ranked core enrichment genes are shown on graphs. (**c**) UMAP plots of single-cell RNA sequencing based on GSE241132 reveal dynamic cellular compositions at different time points during human wound healing. (**d**) Violin plot of spatiotemporal dynamic NLRP3 expression in wound tissues during wound healing. (**e**) Expression patterns of IL-1 signaling pathway-related ligand-receptor across different cell types during wound healing. (**f**) UMAP plots of macrophage subtypes during wound healing. (**g**) Dot plot of NLRP3-related genes expression (*NLRP3*, *IL-1β*, and *CASP1*) in macrophage subtypes. (**h**) Dot plot of NLRP3-related genes expression (NLRP3, IL-1β, and CASP1) in macrophage of cluster3 during wound healing. (**i**) KEGG enrichment analysis of macrophage cluster 3. *Epi* epidermal, *SMC* smooth muscle cell, *MEL* melanocyte, *LC* langerhans cell, *HF* hair follicle

Downloaded from academic.oup.com/burnstrauma/article/doi/10.1093/burnst/tkag002/8415534 by guest on 12 October 2026

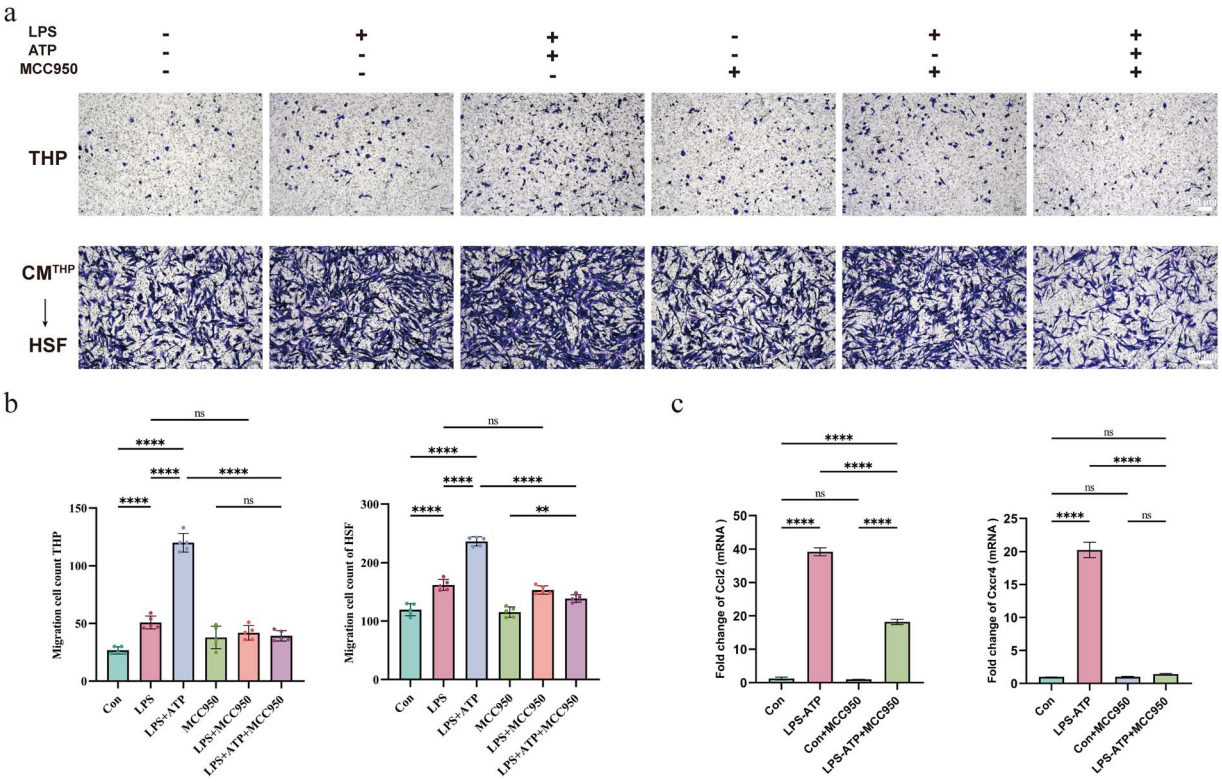


Figure 13 NLRP3 inflammasome activation orchestrates the migratory capacity of human macrophages and dermal fibroblasts. (**a**) Representative crystal violet staining images in transwell assays to evaluate NLRP3 inflammasome activation on THP cells migration and the effect of macrophage NLRP3 inflammasome activation on HSFs migration. Scale bar, 100 μm. (**b**) Quantitative analysis of THP-1 and HSF cell migration numbers (mean ± SD, $n = 3$). (**c**) qRT-PCR analysis of NLRP3 inflammasome activation on the chemotaxis-related genes CCL2 and CXCR4 in THP-1 cells (mean ± SD, $n = 3$). *CM* conditioned medium, *HSF* human skin fibroblast, *HPF* high power field

the chemotaxis-associated genes *CCL2* and *CXCR4*, suggesting that NLRP3-dependent THP-1 migration and its pro-migratory influence on HSFs are partly mediated through these chemokine pathways (Figure 13b and c). Collectively, these data mirror our murine *in vitro* findings and establish that NLRP3 inflammasome activation is likewise indispensable for the migratory behavior of human macrophages and fibroblasts.

Discussion

This study establishes the NLRP3 inflammasome as a spatiotemporal orchestrator of wound healing, balancing inflammation-driven repair with regenerative outcomes. Using Nlrp3 −/− mice, multi-omics, and human validation, we demonstrate that NLRP3 activation during the inflammatory phase recruits macrophages and fibroblasts via CCL/CXCL chemokines, while its suppression in later phases facilitates M2 macrophage polarization and tissue repair. Mechanistically, NLRP3 governs fibroblast phenotypic plasticity through IL-1 signaling, linking early inflammation to ECM remodeling. After the inflammatory wave subsides, macrophage inflammasome activity declines, NLRP3-independent intrinsic pathways become more prominent. These pro-inflammatory fibroblasts display heightened responsiveness to late-stage TGF-β1, which via NLRP3/ROS axis augment TGF-β/Smad signaling and promotes fibroblast differentiation into myo fibroblasts. These findings resolve the paradox of NLRP3's dual roles—essential for acute repair but detrimental in chronic wounds—and propose phase-specific targeting as a therapeutic strategy.

Our data reveal that NLRP3 activation in both macrophages and fibroblasts drives chemokine expression, essential for recruiting immune and stromal cells to the wound site (Figure 4). Transwell assays confirmed that NLRP3-activated macrophages potently enhance fibroblast migration—an effect abolished by the NLRP3 inhibitor MCC950. This aligns with prior work showing fibroblast-mediated macrophage recruitment by CCL2 but extends these findings by implicating NLRP3 as an upstream regulator of chemotaxis [15]. Notably, NLRP3-positive fibroblasts, transiently elevated during inflammation, exhibited chemotaxis-related gene enrichment, suggesting a self-reinforcing loop where NLRP3 primes fibroblasts to amplify recruitment signals (Figure 6i and j). Pro-inflammatory fibroblasts are crucial for recruiting themselves and immune cells, including macrophages, and can serve as precursors to myo fibroblasts in the later stages of wound healing [30].

As a pivotal regulator of immunity and inflammation, NLRP3 deficiency significantly downregulated pro-inflammatory genes and upregulated anti-inflammatory genes in wounds, not only during the inflammatory phase but also during the proliferative phase (Figure 5a and b). The expression of these genes is crucial for regulating the pro- and anti-inflammatory phenotypes of macrophages. Our *in vitro* and *in vivo* experiments confirmed the negative correlation between NLRP3 and the anti-inflammatory phenotype of macrophages. NLRP3 KO promotes the switching of macrophages to the anti-inflammatory M2 phenotype.

Downloaded from academic.oup.com/burnstrauma/article/doi/10.1093/burnst/tkag002/8415534 by guest on 12 October 2026

Further analysis of single-cell sequencing data of mouse wound healing showed that NLRP3 upregulation promotes macrophage recruitment and M1 polarization. High NLRP3 expression in fibroblasts enhances their pro-inflammatory phenotype and chemotaxis but inhibits collagen remodeling and repair (Figure 6). This aligns with prior studies, namely, NLRP3 inflammasome activation promotes macrophage M1 polarization [25, 26, 36], and pro-inflammatory fibroblasts show traits of myo fibroblast phenotype suppression [12, 19, 30]. Single-cell pseudotime analysis identified two fibroblast trajectories: pro-inflammatory (IL-1β-high) and reparative (Myoc-high). NLRP3 deficiency disrupted this bifurcation, reducing reparative gene expression (e.g. Acta2, Col1a1). Co-culture experiments revealed that macrophage inflammasome activation could further promote NLRP3 in fibroblasts, suppressing their reparative function—a mechanism reduced in Nlrp3 −/− fibroblasts. This feedforward loop partly align with studies focusing on fibroblast-autonomous NLRP3 roles [37], highlighting our work's novelty in defining intercellular crosstalk as a critical driver of fibroblast plasticity.

NLRP3 displays varying expression levels across different tissues and cell types, contributing to chronic inflammation-driven pathologies in multiple organ systems [36, 38]. While its mechanisms in immune cells have been extensively characterized, its functions in non-immune cells remain an area of active investigation with some contradictory findings. For instance, In cardiac fibrosis associated with heart failure, Bracey et al. demonstrated that mitochondrial-localized NLRP3 protein can promote Smad signaling and myocardial fibrosis through reactive oxygen species (ROS) generation, independently of inflammasome assembly [33]. Concurrently, Yasutomi et al. reported that ATP released from sympathetic efferent nerves activates the P2X7 receptor on cardiomyocytes, leading to NLRP3 inflammasome activation, IL-1β production, and adaptive cardiac hypertrophy [39]. Similarly, in renal pathology, emerging evidence highlights inflammasome-independent functions of NLRP3 in chronic kidney disease (CKD) pathogenesis [32]. Anders et al. revealed that NLRP3 protein activates fibroblast TGF-β signaling and promotes nephrocalcinosis-related CKD progression through mechanisms independent of inflammasome formation [31]. In contrast, Cliff et al. emphasized the crucial role of NLRP3 in macrophage-epithelial cell crosstalk during diabetic nephropathy development, underscoring its cell-type-specific functions [40]. Building upon these established paradigms, our study provides evidence that NLRP3 in skin fibroblasts operates through a similar non-canonical mechanism. We demonstrated that NLRP3 enhances mitochondrial ROS production and potentiates TGF-β-induced Smad signaling pathway activation independently of inflammasome formation. Genetic ablation of NLRP3 attenuated Smad pathway activation and consequently reduced fibrosis (Figure 8). Furthermore, our findings partially elucidate the stage-specific regulatory functions of NLRP3 during the inflammatory and proliferative phases of wound healing, particularly its coordinated actions in modulating both macrophage polarization and fibroblast activation, revealing a sophisticated intercellular communication network that orchestrates tissue repair versus fibrosis.

During the proliferative phase at wound post-injury Day 7, NLRP3 suppression correlated with M2 macrophage polarization and upregulated regenerative pathways, including Wnt/Notch signaling. NLRP3 deficiency accelerated this shift, resulting in reduced fibrosis and enhanced repair of hair follicles and nerves. Similar to fetal models, Nlrp3 KO mice retained relatively low inflammation and high anti-inflammatory macrophage. This aligns with Walraven et al.'s observations that fetal wounds with higher M2 polarization (∼80% in fetal versus 60% in adult wounds) achieve high-quality regeneration when the inflammatory burden is minimized [41, 42]. The process of hair follicle regeneration is intricately regulated by the immune system. Emerging evidence indicates that RNase L activates the NLRP3 inflammasome, leading to caspase-1 activation, which in turn suppresses TLR3-mediated signaling—a pathway critical for wound-induced hair follicle neogenesis (WHIN) [43]. Consequently, inhibition of caspase-1 promotes WHIN, a finding consistent with the enhanced hair follicle appearance observed in our NLRP3-deficient mice (Figure 9). Furthermore, hair follicle regeneration is known to be modulated by regulatory T cells (Tregs) [44, 45], and NLRP3 has been implicated in regulating Th17 cell function and their plasticity toward a Treg phenotype [46, 47]. Collectively, these findings suggest a mechanistic link whereby NLRP3 suppression may foster a permissive immune microenvironment, which characterized by altered caspase-1 activity and enhanced Treg regulation that actively supports hair follicle regeneration.

IL-1β is the cardinal downstream effector unleashed by NLRP3 inflammasome activation. In WT mice, antibody-mediated IL-1β restriction markedly curtailed neutrophil and macrophage infiltration during the inflammatory phase, arrested the macrophage pro-inflammatory switch, postponed wound closure, and paradoxically intensified fibrosis in the remodeling stage (Figures 10, S7, and 8). Conversely, local IL-1β reconstitution in NLRP3-deficient animals partially rescued the blunted recruitment of inflammatory and reparative cells and accelerated closure, yet ultimately drove excessive scar formation (Figures 11, S9, and 10). These observations echo prior work linking IL-1β to leukocyte trafficking and chronic inflammation [35]; however, our integrative functional assays and multi-omics analyses uniquely identify NLRP3, acting upstream of IL-1β as the master role of choreographing wound chemotaxis and orchestrating the dynamic phenotypic transitions of macrophages and fibroblasts throughout the healing process.

Analysis of human wound RNA-seq data corroborates the conserved dynamic expression pattern of NLRP3 observed in mouse wounds, showing elevated levels in chronic wounds such as venous ulcers, with expression peaking in macrophages during repair. Furthermore, an NLRP3-high macrophage cluster was found to upregulate genes related to chemotaxis and migration (Figure 12). *In vitro* results further indicated that NLRP3 inflammasome activation is indispensable for the migratory capacity of both human macrophages and fibroblasts. Recent studies demonstrate that hydrogel-based delivery of therapeutics targeting NLRP3-mediated chronic inflammation promotes diabetic wound healing [48, 49]. However, as highlighted in our study, excessive inhibition of NLRP3 during the inflammatory phase may impair the migration of immune cells and pro-repair cells to the wound site, thereby compromising healing. Therefore, future research on NLRP3-targeted wound therapies should pay close attention to its spatiotemporal regulatory mechanisms [9, 50–52].

Collectively, our findings position the NLRP3 inflammasome as a contextual rheostat of cutaneous repair. In acute wounds, a transient burst of NLRP3 activity within the early inflammatory

Downloaded from academic.oup.com/burnstrauma/article/doi/10.1093/burnst/tkag002/8415534 by guest on 12 October 2026

phase generates an IL-1β gradient that recruits monocyte-derived macrophages and dermal fibroblasts, coordinates a swift M1-to-M2 macrophage transition, and drives fibroblast conversion to a collagen-secretory phenotype, thereby ensuring timely granulation tissue formation and closure. In contrast, chronic diabetic or venous ulcers exhibit sustained NLRP3 hyper-activation that continually releases IL-1β [49, 53, 54]. This arrests macrophages in a non-resolving M1 state and locks fibroblasts into a dysfunctional, pro-inflammatory, senescence-associated secretory phenotype, leading to impaired collagen deposition and angiogenesis and converting the wound into a non-healing niche. Pharmacological NLRP3 inhibition or IL-1β blockade restores M2 signatures, rejuvenates fibroblast ECM production, and accelerates closure, underscoring the therapeutic imperative to calibrate rather than ablate NLRP3 signaling in chronic wounds [48–50, 55].

Limitations and future perspectives

While this study provides insights into the role of NLRP3 in wound healing and regeneration, several limitations warrant consideration. First, although CRISPR-Cas9-mediated gene editing was successfully employed, our study did not utilize comprehensive off-target assessment methods such as Tracking-seq [56], CIRCLE-Seq [57], DISCOVER-Seq [58], or GUIDE-Seq [59]. As emphasized in latest reviews and articles, the combination of at least one bioinformatic prediction tool with one empirical method is essential to minimize the risk of overlooking off-target edits [60]—a standard we acknowledge was not fully met. Future studies would benefit from implementing these rigorous validation protocols to conclusively rule out potential confounding effects from unintended genomic modifications.

Second, the experimental design involved a relatively constrained sample size. To maintain genetic homogeneity, we utilized littermate controls of the same sex across three experimental groups at five critical time points, resulting in a group size of $n = 4$. While this approach controlled for biological variability, it falls below the conventional standard of $n = 6$–8 for animal studies and may consequently increase the risk of false-positive observations. Future replication with larger cohort sizes would enhance the statistical robustness of our findings.

A particular limitation was the decision not to employ a wound-edge fixation device in our murine model [61]. The consequent wound contraction makes it difficult to definitively exclude the possibility that pre-existing hair follicles and other adjacent structures were pulled into the wound bed, rather than resulting from genuine de novo regeneration. To conclusively address this limitation and elucidate the specific role of NLRP3 in hair follicle regeneration, we propose two key approaches for future investigation: (i) employing silicone-ring splints to fully inhibit wound contraction, thereby enabling unambiguous confirmation of follicular neogenesis [62]; and (ii) utilizing lineage-tracing models to precisely track the origin and differentiation pathways of epithelial stem cells during wound repair [63].

Beyond the specific focus on NLRP3, emerging evidence suggests other inflammasome complexes may contribute to wound healing pathophysiology. While NLRP3 and NLRP1 sense pathogens and damage signals indirectly, other inflammasomes including NAIP, AIM2, and NLRP6 can directly recognize PAMPs or DAMPs [64]. Recent studies have revealed potential roles for AIM2 and NLRC4 inflammasomes in tissue repair. The AIM2 inflammasome, activated by cytosolic DNA, has been shown to respond to mitochondrial DNA release following tissue injury, thereby amplifying inflammatory signaling [65]. Additionally, NAIP/NLRC4 can induce pyroptosis in macrophages and pulmonary fibroblasts, contributing to acute lung injury [66]. Furthermore, studies demonstrate that AIM2 and NLRC4 can drive acute brain injury independently of NLRP3 [67]. The potential crosstalk and compensatory mechanisms among these inflammasomes suggest a more complex regulatory network than currently understood. Future investigations using single-cell transcriptomics and cell-specific KO models should aim to delineate the spatiotemporal dynamics and relative contributions of different inflammasome complexes across various healing phases and cellular populations.

While our initial screening of NLRP3 as a key candidate utilized sequencing data from 1 mm wounds, we employed the more commonly used 8 mm wound model for detailed experimental observation of the healing process. Studies indicate that although wound size in murine models does not significantly alter the fundamental stages of healing, it can influence adaptive immune responses and fibroblast heterogeneity, particularly affecting WIHN [68–70]. Importantly, our experimental validation in the 8 mm murine wound model demonstrates that the candidate genes and pathways identified through in-silico analysis of the GSE23006 dataset show consistent and significant trends across different wound sizes. This convergence suggests that the NLRP3 inflammasome's spatiotemporal regulation of macrophage and fibroblast activity represents a fundamental mechanism in acute wound healing, largely independent of specific wound dimensions.

Finally, while our findings highlight NLRP3 as a promising therapeutic target, significant questions remain regarding its spatiotemporal regulation in human wound healing. A deeper understanding of its cell-type-specific functions, interaction networks, and activity modulation is essential for developing precise therapeutic strategies. The ultimate challenge—and exciting opportunity—lies in balancing the beneficial roles of NLRP3 in acute repair with its detrimental contributions to chronic inflammation and fibrosis. Future research should focus on developing temporal-specific targeting approaches that can harness its protective functions while mitigating its pathological effects, thereby advancing new treatment paradigms for chronic wounds and scarring.

Conclusions

Our study reveals a temporally ordered and cell-specific expression pattern of NLRP3 during wound healing. In the inflammatory phase, NLRP3 is predominantly expressed in macrophages, where canonical inflammasome activation releases IL-1β. This macrophage-derived IL-1β not only amplifies the recruitment of macrophages and fibroblasts but also transiently suppresses the pro-reparative phenotype in fibroblasts. Concurrently, IL-1β upregulates NLRP3 expression within fibroblasts, promoting their shift toward a pro-inflammatory state. As inflammation resolves, a distinct, inflammasome-independent mechanism emerges: these pro-inflammatory fibroblasts, which accumulate high levels of NLRP3 and ROS, exhibit heightened sensitivity to TGF-β1. This facilitates TGF-β/Smad signaling activation and ultimately

Downloaded from academic.oup.com/burnstrauma/article/doi/10.1093/burnst/tkag002/8415534 by guest on 12 October 2026

promotes myo fibroblast differentiation during the later stages of repair.

Abbreviations

NLRP3: NOD-like receptor family pyrin domain-containing 3; PAMPs: Pathogen-associated molecular patterns; DAMPs: Damage-associated molecular patterns; ECM: Extracellular matrix; WT: Wild-type; KO: Knockout; NHEJ: Non-homologous end-joining; DMEM: Dulbecco's Modified Eagle Medium; M-CSF: Macrophage colony-stimulating factor; LPS: lipopolysaccharide; IL-4: Interleukin-4; HSF: Human skin fibroblast; H&E: Hematoxylin and eosin; IHC: immunohistochemistry; HRP: Horseradish peroxidase; IF: Immunofluorescence; RT-qPCR: Quantitative real-time PCR. DEGs: Differentially expressed genes; GO: Gene Ontology; FDR: False discovery rate; PCA: Principal component analysis; COLI: Collagen type I; α-SMA: α-smooth muscle actin; DC: dendritic cell.

Acknowledgements

We thank Prof. Nanbo Liu (Southern Medical University, Guangdong Provincial People's Hospital) for the generous donation of the Nlrp3 KO mouse.

Author contributions

Dongzhen Zhu (Conceptualization [lead], Data curation [lead], Formal analysis [lead], Investigation [lead], Methodology [lead], Project administration [lead], Software [lead], Validation [lead], Visualization [lead], Writing—original draft [lead]), Jianjun Li (Data curation [equal], Methodology [equal], Project administration [equal], Software [equal], Visualization [equal], Validation, Data curation), Bingyang Yu (Conceptualization [equal], Methodology [equal], Project administration [equal], Validation [equal], Formal analysis, Data curation), Nanbo Liu (Investigation [equal], Resources [supporting], Supervision [equal], Methodology), Xu Guo (Project administration [equal], Visualization [equal], Methodology, Investigation), Yanlin Su (Conceptualization [equal], Investigation [equal], Supervision [equal], Methodology), Yuzhen Wang (Methodology [equal], Project administration [equal]), Yuyan Huang (Data curation [equal], Methodology [equal]), Liting Liang (Data curation [equal], Visualization [equal], Methodology), Linhao Hou (Formal analysis [equal], Methodology), Chao Zhang (Formal analysis [equal], Methodology [equal], Conceptualization, Visualization), Qinghua Liu (Project administration [supporting], Conceptualization, Visualization), Mengde Zhang (Project administration [supporting], Conceptualization, Visualization), Wei Song (Resources [equal], Methodology), Yi Kong (Funding acquisition [equal], Supervision [equal], Software), Jinpeng Du (Visualization [equal], Investigation, Data curation), Zhao Li (Funding acquisition [equal], Supervision [equal], Conceptualization), Yue Kong (Investigation [equal], Visualization [equal]), Feng Tian (Software [equal], Visualization [equal]), Xiangye Yin (Visualization [equal]), Ping Zhu (Funding acquisition [equal], Investigation [equal], Resources [equal], Methodology), Xiao-Bing Fu (Funding acquisition [equal], Writing—review & editing [equal], Conceptualization, Resources, Supervision, Project administration), and Sha Huang (Conceptualization [lead], Funding acquisition [lead], Resources [lead], Supervision [lead], Writing—review & editing [lead], Project administration)

Supplementary material

Supplementary material is available at *Burns & Trauma Journal* online.

Ethics approval and consent to participate

All the animal experiments were performed according to the guidelines and approved by the Animal Ethics Committee of the Chinese PLA General Hospital (approval no. S2024-407-01).

Conflict of interest

The authors declare that they have no competing financial interests or personal relationships that may have influenced the work reported in this study.

Funding

This study was supported by the National Key Research and Development Program of China (2022YFA1104600, 2022YFA1104604), the National Nature Science Foundation of China (82472166, 32471432, 82372158, U24A20374), the Military Medical Research Projects, the Science Fund for National Defense Distinguished Young Scholars, Beijing Natural Science Foundation (L234066), and the Innovation Cultivation Fund of the Sixth Medical Center, Chinese PLA General Hospital (CXPY202210).

Data availability

The data supporting the findings of this study are available from the corresponding author upon reasonable request.

References

1. Peña OA, Martin P. Cellular and molecular mechanisms of skin wound healing. *Nat Rev Mol Cell Biol* 2024;25:599–616. https://doi.org/10.1038/s41580-024-00715-1.
2. Cañedo-Dorantes L, Cañedo-Ayala M. Skin acute wound healing: a comprehensive review. *Int J Inflamm* 2019;2019:1–15. https://doi.org/10.1155/2019/3706315.
3. Martin P, Pardo-Pastor C, Jenkins RG, Rosenblatt J. Imperfect wound healing sets the stage for chronic diseases. *Science* 2024;386:eadp2974. https://doi.org/10.1126/science.adp2974.
4. Monaghan MG, Borah R, Thomsen C, Browne S. Thou shall not heal: overcoming the non-healing behaviour of diabetic foot ulcers by engineering the inflammatory microenvironment. *Adv Drug Deliv Rev* 2023;203:115120. https://doi.org/10.1016/j.addr.2023.115120.
5. Artlett CM. Inflammasomes in wound healing and fibrosis. *J Pathol* 2013;229:157–67. https://doi.org/10.1002/path.4116.
6. Akbal A, Dernst A, Lovotti M, Mangan MSJ, McManus RM, Latz E. How location and cellular signaling combine to activate the NLRP3 inflammasome. *Cell Mol Immunol* 2022;19:1201–14. https://doi.org/10.1038/s41423-022-00922-w.

Downloaded from academic.oup.com/burnstrauma/article/doi/10.1093/burnst/tkag002/8415534 by guest on 12 October 2026

7. Swanson KV, Deng M, Ting JP-Y. The NLRP3 inflammasome: molecular activation and regulation to therapeutics. *Nat Rev Immunol* 2019;19:477–89. https://doi.org/10.1038/s41577-019-0165-0.
8. Vinaik R, Abdullahi A, Barayan D, Jeschke MG. NLRP3 inflammasome activity is required for wound healing after burns. *Transl Res* 2020;217:47–60. https://doi.org/10.1016/j.trsl.2019.11.002.
9. Ding Y, Ding X, Zhang H, Li S, Yang P, Tan Q. Relevance of NLRP3 Inflammasome-related pathways in the pathology of diabetic wound healing and possible therapeutic targets. *Oxidative Med Cell Longev* 2022;2022:1–15. https://doi.org/10.1155/2022/9687925.
10. Huang C, Ogawa R. Role of Inflammasomes in keloids and hypertrophic scars—lessons learned from chronic diabetic wounds and skin fibrosis. *IJMS* 2022;23:6820. https://doi.org/10.3390/ijms23126820.
11. Pyrillou K, Burzynski LC, Clarke MCH. Alternative pathways of IL-1 activation, and its role in health and disease. *Front Immunol* 2020;11:613170. https://doi.org/10.3389/fimmu.2020.613170.
12. Tsukui T, Wolters PJ, Sheppard D. Alveolar fibroblast lineage orchestrates lung inflammation and fibrosis. *Nature* 2024;631:627–34. https://doi.org/10.1038/s41586-024-07660-1.
13. Bünemann E, Hoff N-P, Buhren BA, Wiesner U, Meller S, Bölke E. *et al.* Chemokine ligand–receptor interactions critically regulate cutaneous wound healing. *Eur J Med Res* 2018;23:4. https://doi.org/10.1186/s40001-017-0299-0.
14. Ridiandries A, Tan JTM, Bursill CA. The role of chemokines in wound healing. *IJMS* 2018;19:3217. https://doi.org/10.3390/ijms19103217.
15. Amuso VM, Haas MR, Cooper PO, Chatterjee R, Hafiz S, Salameh S. *et al.* Fibroblast-mediated macrophage recruitment supports acute wound healing. *J Invest Dermatol* 2024;145:1781–1797.e8. https://doi.org/10.1016/j.jid.2024.10.609.
16. Jin L, Zhou S, Zhao S, Long J, Huang Z, Zhou J. *et al.* Early short-term hypoxia promotes epidermal cell migration by activating the CCL2-ERK1/2 pathway and epithelial-mesenchymal transition during wound healing. *Burns Trauma* 2024;12:tkae017. https://doi.org/10.1093/burnst/tkae017.
17. Duan X, Yuan X, Yao B, Song W, Li Z, Enhejirigala. *et al.* The role of CTHRC1 in promotion of cutaneous wound healing. *Signal Transduct Target Ther* 2022;7:183. https://doi.org/10.1038/s41392-022-01008-9.
18. Chen L, Arbieva ZH, Guo S, Marucha PT, Mustoe TA, DiPietro LA. Positional differences in the wound transcriptome of skin and oral mucosa. *BMC Genomics* 2010;11:471. https://doi.org/10.1186/1471-2164-11-471.
19. Sinha S, Sparks HD, Labit E, Robbins HN, Gowing K, Jaffer A. *et al.* Fibroblast inflammatory priming determines regenerative versus fibrotic skin repair in reindeer. *Cell* 2022;185:4717–4736.e25. https://doi.org/10.1016/j.cell.2022.11.004.
20. Hu KH, Kuhn NF, Courau T, Tsui J, Samad B, Ha P. *et al.* Transcriptional space-time mapping identifies concerted immune and stromal cell patterns and gene programs in wound healing and cancer. *Cell Stem Cell* 2023;30:885–903.e10. https://doi.org/10.1016/j.stem.2023.05.001.
21. Mascharak S, Talbott HE, Januszyk M, Griffin M, Chen K, Davitt MF. *et al.* Multi-omic analysis reveals divergent molecular events in scarring and regenerative wound healing. *Cell Stem Cell* 2022;29:315–327.e6. https://doi.org/10.1016/j.stem.2021.12.011.
22. Liu Z, Bian X, Luo L, Björklund ÅK, Li L, Zhang L. *et al.* Spatiotemporal single-cell roadmap of human skin wound healing. *Cell Stem Cell* 2024;32:479–498.e8. https://doi.org/10.1016/j.stem.2024.11.013.
23. Cai Y, Xiong M, Xin Z, Liu C, Ren J, Yang X. *et al.* Decoding aging-dependent regenerative decline across tissues at single-cell resolution. *Cell Stem Cell* 2023;30:1674–1691.e8. https://doi.org/10.1016/j.stem.2023.09.014.
24. Krzyszczyk P, Schloss R, Palmer A, Berthiaume F. The role of macrophages in acute and chronic wound healing and interventions to promote pro-wound healing phenotypes. *Front Physiol* 2018;9:419. https://doi.org/10.3389/fphys.2018.00419.
25. Z J, L X, W C, L Y, W Y, M C. *et al.* NLRP3 inflammasome mediates M1 macrophage polarization and IL-1β production in inflammatory root resorption. *J Clin Periodontol* 2020;47:451–60. https://doi.org/10.1111/jcpe.13258.
26. SIRT1 Promotes M2 Microglia Polarization via Reducing ROS-Mediated NLRP3 Inflammasome Signaling After Subarachnoid Hemorrhage - PubMed https://pubmed.ncbi.nlm.nih.gov/34899720/ (accessed 6 October 2024).
27. Wang Y, Wan L, Zhang Z, Li J, Qu M, Zhou Q. Topical calcitriol application promotes diabetic corneal wound healing and reinnervation through inhibiting NLRP3 inflammasome activation. *Exp Eye Res* 2021;209:108668. https://doi.org/10.1016/j.exer.2021.108668.
28. Shapouri-Moghaddam A, Mohammadian S, Vazini H, Taghadosi M, Esmaeili S-A, Mardani F. *et al.* Macrophage plasticity, polarization, and function in health and disease. *J Cell Physiol* 2018;233:6425–40. https://doi.org/10.1002/jcp.26429.
29. Jiang D, Guo R, Machens H-G, Rinkevich Y. Diversity of fibroblasts and their roles in wound healing. *Cold Spring Harb Perspect Biol* 2023;15:a041222. https://doi.org/10.1101/cshperspect.a041222.
30. CD201+ fascia progenitors choreograph injury repair—PubMed https://pubmed.ncbi.nlm.nih.gov/37968392/ (24 accessed April 2025).
31. Anders H-J, Suarez-Alvarez B, Grigorescu M, Foresto-Neto O, Steiger S, Desai J. *et al.* The macrophage phenotype and inflammasome component NLRP3 contributes to nephrocalcinosis-related chronic kidney disease independent from IL-1-mediated tissue injury. *Kidney Int* 2018;93:656–69. https://doi.org/10.1016/j.kint.2017.09.022.
32. Mulay SR. Multifactorial functions of the inflammasome component NLRP3 in pathogenesis of chronic kidney diseases. *Kidney Int* 2019;96:58–66. https://doi.org/10.1016/j.kint.2019.01.014.
33. Bracey NA, Gershkovich B, Chun J, Vilaysane A, Meijndert HC, Wright JR. *et al.* Mitochondrial NLRP3 protein induces reactive oxygen species to promote Smad protein signaling and fibrosis independent from the inflammasome. *J Biol Chem* 2014;289:19571–84. https://doi.org/10.1074/jbc.M114.550624.
34. Alexanian M, Padmanabhan A, Nishino T, Travers JG, Ye L, Pelonero A. *et al.* Chromatin remodelling drives immune

Downloaded from academic.oup.com/burnstrauma/article/doi/10.1093/burnst/tkag002/8415534 by guest on 12 October 2026

cell-fibroblast communication in heart failure. *Nature* 2024;635:434–43. https://doi.org/10.1038/s41586-024-08085-6.
35. Xie X, Wang P, Jin M, Wang Y, Qi L, Wu C. *et al.* IL-1β-induced epithelial cell and fibroblast transdifferentiation promotes neutrophil recruitment in chronic rhinosinusitis with nasal polyps. *Nat Commun* 2024;15:9101. https://doi.org/10.1038/s41467-024-53307-0.
36. Mangan MSJ, Olhava EJ, Roush WR, Seidel HM, Glick GD, Latz E. Targeting the NLRP3 inflammasome in inflammatory diseases. *Nat Rev Drug Discov* 2018;17:688. https://doi.org/10.1038/nrd.2018.149.
37. Li H, Wang Z, Zhou F, Zhang G, Feng X, Xiong Y. *et al.* Sustained activation of NLRP3 inflammasome contributes to delayed wound healing in aged mice. *Int Immunopharmacol* 2023;116:109828. https://doi.org/10.1016/j.intimp.2023.109828.
38. Nagar A, Bharadwaj R, Mof S, Roy A. What are NLRP3-ASC specks? An experimental progress of 22 years of inflammasome research. *Front Immunol* 2023;14:1188864. https://doi.org/10.3389/fimmu.2023.1188864.
39. Higashikuni Y, Liu W, Numata G, Tanaka K, Fukuda D, Tanaka Y. *et al.* NLRP3 Inflammasome activation through heart-brain interaction initiates cardiac inflammation and hypertrophy during pressure overload. *Circulation* 2023;147:338–55. https://doi.org/10.1161/CIRCULATIONAHA.122.060860.
40. Cliff CL, Squires PE, Hills CE. Tonabersat suppresses priming/activation of the NOD-like receptor protein-3 (NLRP3) inflammasome and decreases renal tubular epithelial-to-macrophage crosstalk in a model of diabetic kidney disease. *Cell Commun Signal* 2024;22:351. https://doi.org/10.1186/s12964-024-01728-1.
41. Walraven M, Talhout W, Beelen RHJ, van Egmond M, Ulrich MMW. Healthy human second-trimester fetal skin is deficient in leukocytes and associated homing chemokines. *Wound Repair Regen* 2016;24:533–41. https://doi.org/10.1111/wrr.12421.
42. Hu MS, Borrelli MR, Hong WX, Malhotra S, Cheung ATM, Ransom RC. *et al.* Embryonic skin development and repair. *Organogenesis* 2018;14:46–63. https://doi.org/10.1080/15476278.2017.1421882.
43. Kirby CS, Islam N, Wier E, Alphonse MP, Sweren E, Wang G. *et al.* RNase L represses hair follicle regeneration through altered innate immune signaling. *J Clin Invest* 2025;135:e172595. https://doi.org/10.1172/JCI172595.
44. Accogli T, Hibos C, Milian L, Geindreau M, Richard C, Humblin E. *et al.* The intrinsic expression of NLRP3 in Th17 cells promotes their protumor activity and conversion into Tregs. *Cell Mol Immunol* 2025;22:541–56. https://doi.org/10.1038/s41423-025-01281-y.
45. Ali N, Zirak B, Rodriguez RS, Pauli ML, Truong H-A, Lai K. *et al.* Regulatory T cells in skin facilitate epithelial stem cell differentiation. *Cell* 2017;169:1119–1129.e11. https://doi.org/10.1016/j.cell.2017.05.002.
46. Liu Z, Hu X, Liang Y, Yu J, Li H, Shokhirev MN. *et al.* Glucocorticoid signaling and regulatory T cells cooperate to maintain the hair-follicle stem-cell niche. *Nat Immunol* 2022;23:1086–97. https://doi.org/10.1038/s41590-022-01244-9.
47. Liu X, Chen J, Yue S, Zhang C, Song J, Liang H. *et al.* NLRP3-mediated IL-1β in regulating the imbalance between Th17 and Treg in experimental autoimmune prostatitis. *Sci Rep* 2024;14:18829. https://doi.org/10.1038/s41598-024-69512-2.
48. Sun J, Jia W, Qi H, Huo J, Liao X, Xu Y. *et al.* An Antioxidative and active shrinkage hydrogel Integratedly promotes Re-epithelization and skin constriction for enhancing wound closure. *Adv Mater* 2024;36:e2312440. https://doi.org/10.1002/adma.202312440.
49. Mao J, Xia W, Wu Y, Li M, Zhao Y, Zhai P. *et al.* Biosynthesis of Lysosomally escaped apoptotic bodies inhibits Inflammasome synthesis in macrophages. *Research (Wash D C)* 2025;8:0581. https://doi.org/10.34133/research.0581.
50. Yang Y, Chen N, Fan J, Fan L, Cai Y, Xue L. *et al.* Spatiotemporal immunomodulation of macrophages via NLRP3/IL-1β pathway by Core-Shell microneedles to promote healing of biofilm-infected diabetic ulcers. *Small* 2025;21:e2505179. https://doi.org/10.1002/smll.202505179.
51. Lv D, Cao X, Zhong L, Dong Y, Xu Z, Rong Y. *et al.* Targeting phenylpyruvate restrains excessive NLRP3 inflammasome activation and pathological inflammation in diabetic wound healing. *Cell Reports Medicine* 2023;4:101129. https://doi.org/10.1016/j.xcrm.2023.101129.
52. Mu X, Wu X, He W, Liu Y, Wu F, Nie X. Pyroptosis and inflammasomes in diabetic wound healing. *Front Endocrinol* 2022;13:950798. https://doi.org/10.3389/fendo.2022.950798.
53. Wolf SJ, Audu CO, Moon JY, Joshi AD, Melvin WJ, Barrett EC. *et al.* Diabetic wound keratinocytes induce macrophage JMJD3-mediated Nlrp3 expression via IL-1R signaling. *Diabetes* 2024;73:1462–72. https://doi.org/10.2337/db23-0968.
54. Liu C, Zhang Q, Zhou H, Jin L, Liu C, Yang M. *et al.* GLP-1R activation attenuates the progression of pulmonary fibrosis via disrupting NLRP3 inflammasome/PFKFB3-driven glycolysis interaction and histone lactylation. *J Transl Med* 2024;22:954. https://doi.org/10.1186/s12967-024-05753-z.
55. Yang S, Feng Y, Chen L, Wang Z, Chen J, Ni Q. *et al.* Disulfiram accelerates diabetic foot ulcer healing by blocking NET formation via suppressing the NLRP3/Caspase-1/GSDMD pathway. *Transl Res* 2023;254:115–27. https://doi.org/10.1016/j.trsl.2022.10.008.
56. Zhu M, Xu R, Yuan J, Wang J, Ren X, Cong T. *et al.* Tracking-seq reveals the heterogeneity of off-target effects in CRISPR-Cas9-mediated genome editing. *Nat Biotechnol* 2025;43:799–810. https://doi.org/10.1038/s41587-024-02307-y.
57. Tsai SQ, Nguyen NT, Malagon-Lopez J, Topkar VV, Aryee MJ, Joung JK. CIRCLE-seq: a highly sensitive in vitro screen for genome-wide CRISPR-Cas9 nuclease off-targets. *Nat Methods* 2017;14:607–14. https://doi.org/10.1038/nmeth.4278.
58. Wienert B, Wyman SK, Richardson CD, Yeh CD, Akcakaya P, Porritt MJ. *et al.* Unbiased detection of CRISPR off-targets in vivo using DISCOVER-Seq. *Science* 2019;364:286–9. https://doi.org/10.1126/science.aav9023.
59. Tsai SQ, Zheng Z, Nguyen NT, Liebers M, Topkar VV, Thapar V. *et al.* GUIDE-seq enables genome-wide profiling of off-target cleavage by CRISPR-Cas nucleases. *Nat Biotechnol* 2015;33:187–97. https://doi.org/10.1038/nbt.3117.
60. Du W, Zhao L, Diao K, Zheng Y, Yang Q, Zhu Z. *et al.* A versatile CRISPR/Cas9 system off-target prediction tool using language model. *Commun Biol* 2025;8:882. https://doi.org/10.1038/s42003-025-08275-6.

Downloaded from academic.oup.com/burnstrauma/article/doi/10.1093/burnst/tkag002/8415534 by guest on 12 October 2026

61. Yampolsky M, Bachelet I, Fuchs Y. Reproducible strategy for excisional skin-wound-healing studies in mice. *Nat Protoc* 2024;19:184–206. https://doi.org/10.1038/s41596-023-00899-4.
62. Wang X, Ge J, Tredget EE, Wu Y. The mouse excisional wound splinting model, including applications for stem cell transplantation. *Nat Protoc* 2013;8:302–9. https://doi.org/10.1038/nprot.2013.002.
63. Dekoninck S, Hannezo E, Sifrim A, Miroshnikova YA, Aragona M, Malfait M. *et al.* Defining the design principles of skin epidermis postnatal growth. *Cell* 2020;181:604–620.e22. https://doi.org/10.1016/j.cell.2020.03.015.
64. Fu J, Schroder K, Wu H. Mechanistic insights from inflammasome structures. *Nat Rev Immunol* 2024;24:518–35. https://doi.org/10.1038/s41577-024-00995-w.
65. Huang X, Li T, Zhang G, Chen J, Li T, Yang S. *et al.* AIM2 activation mediated by RIPK1/3-dependent mitochondrial DNA release drives Aβ1-40-induced retinal pigment epithelium injury. *Cell Commun Signal* 2025;23:301. https://doi.org/10.1186/s12964-025-02294-w.
66. Zhang Y, Zhang G, Dong B, Pandeya A, Cui J, dos S VS. *et al.* Pyroptosis of pulmonary fibroblasts and macrophages through NLRC4 inflammasome leads to acute respiratory failure. *Cell Rep* 2025;44:115479. https://doi.org/10.1016/j.celrep.2025.115479.
67. Denes A, Coutts G, Lénárt N, Cruickshank SM, Pelegrin P, Skinner J. *et al.* AIM2 and NLRC4 inflammasomes contribute with ASC to acute brain injury independently of NLRP3. *Proc Natl Acad Sci USA* 2015;112:4050–5. https://doi.org/10.1073/pnas.1419090112.
68. Abbasi S, Sinha S, Labit E, Rosin NL, Yoon G, Rahmani W. *et al.* Distinct regulatory programs control the latent regenerative potential of dermal fibroblasts during wound healing. *Cell Stem Cell* 2020;27:396–412.e6. https://doi.org/10.1016/j.stem.2020.07.008.
69. Lim CH, Sun Q, Ratti K, Lee S-H, Zheng Y, Takeo M. *et al.* Hedgehog stimulates hair follicle neogenesis by creating inductive dermis during murine skin wound healing. *Nat Commun* 2018;9:4903. https://doi.org/10.1038/s41467-018-07142-9.
70. Yang Y, Chu C, Liu L, Wang C, Hu C, Rung S. *et al.* Tracing immune cells around biomaterials with spatial anchors during large-scale wound regeneration. *Nat Commun* 2023;14:5995. https://doi.org/10.1038/s41467-023-41608-9.

Downloaded from academic.oup.com/burnstrauma/article/doi/10.1093/burnst/tkag002/8415534 by guest on 12 October 2026

© The Author(s) 2026. Published by Oxford University Press. This is an Open Access article distributed under the terms of the Creative Commons Attribution-NonCommercial License (https://creativecommons.org/licenses/by-nc/4.0/), which permits non-commercial re-use, distribution, and reproduction in any medium, provided the original work is properly cited. For commercial re-use, please contact reprints@oup.com for reprints and translation rights for reprints. All other permissions can be obtained through our RightsLink service via the Permissions link on the article page on our site—for further information please contact journals.permissions@oup.com.
Burns & Trauma, 2026, 14, tkag002
https://doi.org/10.1093/burnst/tkag002
Research Article